

AD706035

MEMORANDUM

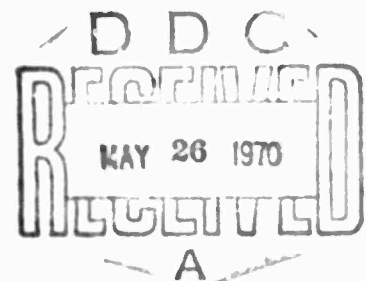
RM-6211-ARPA

APRIL 1970

**STUDIES IN CLIMATE DYNAMICS FOR  
ENVIRONMENTAL SECURITY: Numerical Studies of  
Transient Planetary Circulations in a  
Wind-Driven Ocean on the Sphere**

W. Lawrence Gates

**PREPARED FOR:  
ADVANCED RESEARCH PROJECTS AGENCY**



**The RAND Corporation**  
SANTA MONICA • CALIFORNIA

61

**BEST  
AVAILABLE COPY**

**MEMORANDUM**

**RM-6211-ARPA**

**APRIL 1970**

**STUDIES IN CLIMATE DYNAMICS FOR  
ENVIRONMENTAL SECURITY: Numerical Studies of  
Transient Planetary Circulations in a  
Wind-Driven Ocean on the Sphere**

**W. Lawrence Gates**

This research is supported by the Advanced Research Projects Agency under Contract No. DAHC15 67 C 0141. Views or conclusions contained in this study should not be interpreted as representing the official opinion or policy of Rand or of ARPA.

**DISTRIBUTION STATEMENT**

This document has been approved for public release and sale; its distribution is unlimited.

PREFACE

Meteorological studies suggest that technologically feasible operations might trigger substantial changes in the climate over broad regions of the globe. Depending on their character, location, and scale, these changes might be both deleterious and irreversible. If a foreign power were to bring about such perturbations either overtly or covertly, either maliciously or heedlessly, the results might be seriously detrimental to the security and welfare of this country. So that the United States may react rationally and effectively to any such actions, it is essential that we have the capability to: (1) evaluate all consequences of a variety of possible actions that might modify the climate, (2) detect trends in the global circulation that presage changes in the climate, either natural or artificial, and (3) determine, if possible, means to counter potentially deleterious climatic changes. Our possession of this capability would make incautious experimentation unnecessary, and would tend to deter malicious manipulation. To this end, the Advanced Research Projects Agency initiated a study of the dynamics of climate to evaluate the effect on climate of environmental perturbations. The present Memorandum is a technical contribution to this larger study.

Rand's position on climate and weather modification studies was asserted in its publications RM-3205-NSF and RM-5835-NSF. The approach to understanding the consequences of climate change must consist of many converging paths; and for reasons of safety and economy this approach must take advantage of the growing versatility of computers.

This Memorandum is the third in a series reporting investigations of the wind-driven oceanic circulation, an understanding of which is essential to broadening our knowledge of the ocean/atmosphere interactions that so powerfully influence weather and climate. The work is based on models for solution on high-speed computers. Rand's prior publications on this particular topic are RM-6110-RC and RM-6210-ARPA.

**PRECEDING PAGE BLANK**

### SUMMARY

The time-dependent primitive equations for a shallow homogeneous ocean with a free surface are solved for a bounded basin on the sphere, driven by a steady zonal wind stress and subject to lateral viscous dissipation. These are the vertically integrated equations for a free-surface model, and are integrated to 60 days from an initial state of rest by an explicit centered-difference method with zero-slip lateral boundary conditions. In a series of comparative numerical solutions it is shown that at least a 2-deg resolution is needed to resolve the western boundary currents adequately and to avoid undue distortion of the transient Rossby waves. The  $\beta$ -plane formulation is shown to be an adequate approximation for the mean circulation in the lower and middle latitudes, but noticeably intensifies the transports poleward of about 50 deg and both slows and distorts the transients in the central basin. The influence of the (southern) zonal boundary on the transport solutions is confined to the southernmost gyre, except in the region of the western boundary currents where its influence spreads to the northern edge of the basin by 30 days. The total boundary current transport is shown to be approximately proportional to the zonal width of the basin and independent of the basin's (uniform) depth, while the elevation of the free water surface is inversely proportional to the basin depth, in accordance with linear theory. The introduction of bottom friction has a marked damping effect on the transient Rossby waves, and also reduces the maximum boundary-current transport. The solutions throughout are approximately geostrophic and are only slightly affected by the nonlinear inertial terms for simple assumed vertical profiles of the horizontal current.

The root-mean-square (rms) transport variability during the period 30 to 60 days is concentrated in the southwest portion of the basin through the reflection of the transient Rossby waves from the western shore and has a maximum corresponding to an rms current variability of about  $3 \text{ cm sec}^{-1}$ . The transport variabilities are about 10 percent of the mean zonal transport and more than 100 percent of the mean meridional transport over a considerable region of the western basin (outside

**PRECEDING PAGE BLANK**

the western boundary current regime). Some 99 percent of the total kinetic energy is associated with the zonal mean and standing zonal waves, which are also responsible for the bulk of the meridional transport of zonal angular momentum. Although the transient Rossby waves systematically produce a momentum flux convergence at the latitude of the maximum eastward current, much in the manner of their atmospheric counterparts, this is only a relatively small contribution to the zonal oceanic momentum balance; the bulk of the mean zonal stress is here balanced by a nearly stationary net pressure torque exerted against the meridional boundaries by the wind-raised water. In an ocean without such boundaries the role of the transient circulations may be somewhat more important.

ACKNOWLEDGEMENTS

This research was initiated with the support of the National Science Foundation under contract C-415, and all of the computations were performed under a grant of computer time made available by the National Center for Atmospheric Research. The programming was capably performed by Mr. Al Nelson of Rand.

CONTENTS

PREFACE. . . . .	iii
SUMMARY. . . . .	v
ACKNOWLEDGEMENTS . . . . .	vii
Section	
I. INTRODUCTION . . . . .	1
II. THE DYNAMICAL MODEL. . . . .	2
III. THE NUMERICAL MODEL. . . . .	8
IV. COMPARATIVE NUMERICAL SOLUTIONS--NUMERICAL AND GEOMETRICAL EFFECTS. . . . .	14
Resolution Tests . . . . .	14
Spherical Versus 8-Plane Coordinates . . . . .	18
Effects of the Boundary and Basin Size . . . . .	25
V. COMPARATIVE NUMERICAL SOLUTIONS--PHYSICAL EFFECTS. . .	30
Frictional Effects . . . . .	30
Nonlinear Effects. . . . .	35
Depth Effects. . . . .	37
VI. STATISTICAL PROPERTIES OF THE SOLUTIONS. . . . .	40
Mean and Variability Fields. . . . .	40
Energy Partitioning. . . . .	42
Angular Momentum Flux. . . . .	45
VII. CONCLUSIONS. . . . .	50
REFERENCES . . . . .	52

**PRECEDING PAGE BLANK**



## I. INTRODUCTION

In previous studies (Gates, 1968, 1969) the transverse Rossby wave was shown to be the principal mode of response of a homogeneous ocean to an imposed large-scale wind stress, and the development of the steady circulations was examined with emphasis on the reflection of these transients from the basin's walls. These integrations were made for an ocean of uniform depth on the  $\beta$ -plane, with a modest degree of nonlinearity and a prescribed lateral eddy viscosity. The role of the nonlinear inertial terms and the effects of changes in the viscous dissipation in such a model have been examined by Bryan (1963), while the corresponding effects in a  $\beta$ -plane model with bottom friction have been examined by Veronis (1966c). It is the purpose of the present paper to extend these investigations to the case of a bounded ocean basin on the spherical earth, with particular attention being given to the role of the transient planetary circulations. In addition to examining the frictional and nonlinear effects in the spherical case, a series of comparative numerical integrations will be presented to show the effects of resolution (grid mesh size) changes, and of changes of the basin's dimensions. The present studies of a homogeneous ocean may be viewed as part of a continuing series of experiments which will culminate in the (barotropic) simulation of the circulation of an ocean basin with realistic lateral and bottom geometry. Although there may be important baroclinic effects in the large-scale ocean circulation, the barotropic model may be able to account for most of the variability of large-scale currents (Phillips, 1966a), at least in the open sea of middle latitudes.

**PRECEDING PAGE BLANK**

## II. THE DYNAMICAL MODEL

The dynamical bases of the barotropic model are the horizontal equations of motion and the equation of continuity for an incompressible homogeneous ocean. In the spherical coordinates  $\lambda$  (longitude),  $\phi$  (latitude), and  $z$  (upward) these may be written

$$\begin{aligned} \frac{\partial u}{\partial t} + \frac{u}{a \cos \phi} \frac{\partial u}{\partial \lambda} + \frac{v}{a} \frac{\partial u}{\partial \phi} + w \frac{\partial u}{\partial z} - \frac{uv}{a} \tan \phi = \\ = - \frac{1}{a \rho_0 \cos \phi} \frac{\partial p}{\partial \lambda} + fv + \frac{1}{\rho_0} \frac{\partial \tau_\lambda}{\partial z} + A \nabla_s^2 u \end{aligned} \quad (1)$$

$$\begin{aligned} \frac{\partial v}{\partial t} + \frac{u}{a \cos \phi} \frac{\partial v}{\partial \lambda} + \frac{v}{a} \frac{\partial v}{\partial \phi} + w \frac{\partial v}{\partial z} + \frac{u^2}{a} \tan \phi = \\ = - \frac{1}{a \rho_0} \frac{\partial p}{\partial \phi} - fu + \frac{1}{\rho_0} \frac{\partial \tau_\phi}{\partial z} + A \nabla_s^2 v \end{aligned} \quad (2)$$

where the velocity components are given by

$$u = a \cos \phi \frac{d\lambda}{dt} \quad (3)$$

$$v = a \frac{d\phi}{dt} \quad (4)$$

$$w = \frac{dz}{dt} \quad (5)$$

with  $a$  the earth's radius,  $\rho_0$  the ocean's (uniform) density,  $p$  the pressure,  $f = 2\Omega \sin \phi$  the Coriolis parameter (with  $\Omega$  the earth's angular speed of rotation),  $\tau_\lambda$  and  $\tau_\phi$  the eastward and northward components of the tangential stress,  $A$  the coefficient of lateral eddy viscosity, and  $\nabla_s^2$  the spherical Laplacian. Here we have neglected the terms  $uv/a^{-1}$  and  $2\Omega w \cos \phi$  in (1) and the term  $wv/a^{-1}$  in (2) in order to maintain energetic consistency when the hydrostatic equation

$$\frac{\partial p}{\partial z} = -\rho_0 g \quad (6)$$

is used as the remnant of the vertical equation of motion. These approximations, together with the use of (a) rather than (a + s) as a coefficient in the terms of (1) and (2), have been shown to be consistent with the preservation of angular momentum (Phillips, 1966b). The equation of continuity accompanying (1) and (2) may be written

$$\frac{1}{a \cos \phi} \frac{\partial u}{\partial \lambda} + \frac{1}{a \cos \phi} \frac{\partial}{\partial \phi} (v \cos \phi) + \frac{\partial w}{\partial s} = 0 \quad (7)$$

which expresses the nondivergence of the three-dimensional velocity. Here the extremely small term  $2ve^{-1}$  has been neglected. Using this equation, the advective terms (the second, third, and fourth on the left-hand sides) of (1) and (2) may be rewritten in the "flux forms"

$$\frac{u}{a \cos \phi} \frac{\partial u}{\partial \lambda} + \frac{v}{a} \frac{\partial u}{\partial \phi} + w \frac{\partial u}{\partial s} = \frac{1}{a \cos \phi} \left[ \frac{\partial(u^2)}{\partial \lambda} + \frac{\partial}{\partial \phi} (uv \cos \phi) \right] + \frac{\partial(uw)}{\partial s} \quad (8)$$

$$\frac{u}{a \cos \phi} \frac{\partial v}{\partial \lambda} + \frac{v}{a} \frac{\partial v}{\partial \phi} + w \frac{\partial v}{\partial s} = \frac{1}{a \cos \phi} \left[ \frac{\partial(uv)}{\partial \lambda} + \frac{\partial}{\partial \phi} (v^2 \cos \phi) \right] + \frac{\partial(vw)}{\partial s} \quad (9)$$

We now integrate the system (1), (2), and (7) over the total vertical depth of the hydrostatic ocean, i.e., from the assumed rigid bottom at  $z = -h(\lambda, \phi)$ , at which the boundary condition is

$$w_{-h} = -V_{-h} \cdot \nabla_s h \quad (10)$$

to the free upper surface at  $z = \xi(\lambda, \phi, t)$ , at which the boundary condition is

$$w_{\xi} = \frac{\partial \xi}{\partial t} + V_{\xi} \cdot \nabla_s \xi \quad (11)$$

Here  $v_{-h}$  denotes  $v$  at  $z = -h$ ,  $V_{-h}$  is the horizontal velocity at  $z = -h$  (with corresponding interpretations at the surface  $z = \zeta$ ), and  $\nabla_\theta$  is the spherical gradient operator. Using these conditions, the hydrostatic equation, (6), and the assumption of a uniform surface (atmospheric) pressure at  $z = \zeta$ , and paying particular attention to the variability of the limits of the vertical integration operator, defined as

$$\langle ( ) \rangle = \int_{-h(\lambda, \theta)}^{\zeta(\lambda, \theta, \tau)} ( ) dz \quad (12)$$

the results of the integration of the "flux forms" of (1) and (2) are

$$\begin{aligned} \frac{\partial \langle u \rangle}{\partial \tau} + \frac{1}{a \cos \theta} \left( \frac{\partial}{\partial \lambda} \langle u^2 \rangle + \frac{\partial}{\partial \theta} \langle uv \cos \theta \rangle \right) - \frac{\tan \theta}{a} \langle uv \rangle \\ = - \frac{g(\zeta + h)}{a \cos \theta} \frac{\partial \zeta}{\partial \lambda} + f \langle v \rangle + \frac{1}{\rho_0} (\tau_\lambda^u - \tau_\lambda^b) \\ + \frac{A}{a^2 \cos \theta} \left[ \frac{1}{\cos \theta} \left\langle \frac{\partial^2 u}{\partial \lambda^2} \right\rangle + \left\langle \frac{\partial}{\partial \theta} \left( \cos \theta \frac{\partial u}{\partial \theta} \right) \right\rangle \right] \end{aligned} \quad (13)$$

$$\begin{aligned} \frac{\partial \langle v \rangle}{\partial \tau} + \frac{1}{a \cos \theta} \left( \frac{\partial}{\partial \lambda} \langle uv \rangle + \frac{\partial}{\partial \theta} \langle v^2 \cos \theta \rangle \right) + \frac{\tan \theta}{a} \langle u^2 \rangle \\ = - \frac{g(\zeta + h)}{a \cos \theta} \frac{\partial \zeta}{\partial \theta} - f \langle u \rangle + \frac{1}{\rho_0} (\tau_\theta^v - \tau_\theta^b) \\ + \frac{A}{a^2 \cos \theta} \left[ \frac{1}{\cos \theta} \left\langle \frac{\partial^2 v}{\partial \lambda^2} \right\rangle + \left\langle \frac{\partial}{\partial \theta} \left( \cos \theta \frac{\partial v}{\partial \theta} \right) \right\rangle \right] \end{aligned} \quad (14)$$

Here  $\tau^u$  and  $\tau^b$  denote the surface-wind stress and the tangential stress on the ocean bottom, respectively. A similar integration of the continuity equation, (7), gives

$$\frac{\partial \xi}{\partial t} + \frac{1}{a \cos \phi} \left( \frac{\partial \langle u \rangle}{\partial \lambda} + \frac{\partial \langle v \cos \phi \rangle}{\partial \phi} \right) = 0 \quad (15)$$

The further reduction of the system (13) to (15) hinges upon the introduction of the assumption that the integrals of the quadratic products  $u^2$ ,  $uv$  and  $v^2$  occurring in the inertial terms on the left-hand sides of (13) and (14) may be expressed in terms of the products of the integrals  $\langle u \rangle$  and  $\langle v \rangle$ ; this assumption amounts to a specification of the vertical structure of the horizontal current. Specifically, we shall assume

$$\begin{aligned} \langle u^2 \rangle &= \frac{S}{h} \langle u \rangle^2 \\ \langle uv \rangle &= \frac{S}{h} \langle u \rangle \langle v \rangle \\ \langle v^2 \rangle &= \frac{S}{h} \langle v \rangle^2 \end{aligned} \quad (16)$$

where  $S$  is a "shape factor," assumed to be a dimensionless constant characteristic of the ocean, and  $h$  is the (undisturbed) local ocean depth. The relations (16) are equivalent to assuming that the velocity components vary with  $z$  in a similar fashion in every vertical, but at a rate inversely proportional to the local water depth, i.e.,

$$u = \frac{C}{h} \langle u \rangle, \quad v = \frac{C}{h} \langle v \rangle \quad (17)$$

where  $C$  is a dimensionless function of  $z$  with  $\langle C \rangle = h$ . The shape factor  $S$  may therefore be written

$$S = \frac{\langle C^2 \rangle}{h} = \text{constant} \quad (18)$$

If a current is assumed to decrease linearly toward zero at the ocean bottom, for example, we have  $C = 2(1 + z/h)$  and  $S = 4/3$ , which may be compared with the case of a current uniform over depth for which  $C = S = 1$ . For a parabolic decrease of speed with depth, with a possible reversal of direction in the deeper water ( $C < 0$ ), values of  $S$  from around 2 to 5 may be inferred.

With the approximations (16) and (18) we may write the integrated equations of motion, (13) and (14), in the forms

$$\begin{aligned} \frac{\partial u}{\partial t} = & - \frac{S}{a \cos \phi} \left[ \frac{\partial}{\partial \lambda} \left( \frac{u^2}{h} \right) + \frac{\partial}{\partial \phi} \left( \frac{uv \cos \phi}{h} \right) \right] \\ & - \frac{gh}{a \cos \phi} \frac{\partial \xi}{\partial \lambda} + fv + \frac{Suv \tan \phi}{ah} + \frac{1}{\rho_0} (\tau_{\lambda}^w - \tau_{\lambda}^b) \\ & + \frac{A}{a^2 \cos \phi} \left[ \frac{1}{\cos \phi} \frac{\partial^2 u}{\partial \lambda^2} + \frac{\partial}{\partial \phi} \left( \cos \phi \frac{\partial u}{\partial \phi} \right) \right] \end{aligned} \quad (19)$$

$$\begin{aligned} \frac{\partial v}{\partial t} = & - \frac{S}{a \cos \phi} \left[ \frac{\partial}{\partial \lambda} \left( \frac{uv}{h} \right) + \frac{\partial}{\partial \phi} \left( \frac{v^2 \cos \phi}{h} \right) \right] \\ & - \frac{gh}{a} \frac{\partial \xi}{\partial \phi} - fu - \frac{Su^2 \tan \phi}{ah} + \frac{1}{\rho_0} (\tau_{\phi}^w - \tau_{\phi}^b) \\ & + \frac{A}{a^2 \cos \phi} \left[ \frac{1}{\cos \phi} \frac{\partial^2 v}{\partial \lambda^2} + \frac{\partial}{\partial \phi} \left( \cos \phi \frac{\partial v}{\partial \phi} \right) \right] \end{aligned} \quad (20)$$

Here we have dropped the brackets and written  $u$  and  $v$  for  $\langle u \rangle$  and  $\langle v \rangle$  in the interest of simplicity, and we have introduced the approximation  $\xi \ll h$  in the coefficient of the second (pressure-force) terms on the right-hand sides. We have also assumed that the last (lateral eddy viscosity) terms may be written with sufficient accuracy by freely commuting the  $\partial/\partial \lambda$ ,  $\partial/\partial \phi$ , and  $\langle \rangle$  operators. Together with the continuity equation, (15), now written as

$$\frac{\partial \xi}{\partial t} = - \frac{1}{a \cos \phi} \left( \frac{\partial u}{\partial \lambda} + \frac{\partial (v \cos \phi)}{\partial \phi} \right) \quad (21)$$

these equations now constitute a dynamical system in the volume transport components  $u$  and  $v$  (vertically-integrated speeds) and in the displacement of the free ocean surface  $\xi$ . This system is the dynamical basis of the present barotropic model, although it has been simplified in the integrations presented below by the assumption of a uniform ocean depth, by the neglect of the bottom stress ( $\tau_{\lambda}^b = \tau_{\phi}^b = 0$ ), and by the prescription of a purely zonal surface wind stress. At the rigid (and assumed vertical) lateral walls of the basin a zero-slip boundary condition  $u = v = 0$  is required, from which the tendency of the water height at the boundary may be determined from the continuity equation, (21), in which that part of the transport divergence involving a derivative tangential to the boundary will now vanish.

### III. THE NUMERICAL MODEL

The equations (19) to (21) are approximated on a finite-difference grid scheme in the surface spherical coordinates  $\lambda$  and  $\phi$  as sketched in Fig. 1. Of the many possible ways to assign the variables on the grid points, the method selected here involves the determination of the transport  $u$  and  $v$  at points for which  $(i + j)$  is odd, with the water elevation  $\xi$  determined at the interlocking network of points for which  $(i + j)$  is even. Here  $i$  and  $j$  are integer indices for the longitude  $\lambda$  and latitude  $\phi$  relative to the origin, such that  $\lambda = (i - 1)\Delta\lambda/2$ ,  $\phi = (j - 1)\Delta\phi/2$ , with  $i, j = 1, 2, \dots$ , and  $\Delta\lambda/2$  and  $\Delta\phi/2$  the separations between adjacent grid points. Such a scheme has proven useful in previous studies (Gates, 1968), and is particularly convenient with the zero-slip boundary condition.

Using centered differences in both space and time, and neglecting the bottom stresses, the difference equations for the system (19) to (21) are:

$$\begin{aligned}
 u_{ij}^{n+1} = & -\frac{2S\Delta t}{a \cos \phi_j} \left[ \frac{1}{4\Delta\lambda} (u_{i+1j+1}^n + u_{i+1j-1}^n)^2 - \frac{1}{4\Delta\lambda} (u_{i-1j+1}^n + u_{i-1j-1}^n)^2 \right. \\
 & + \frac{\cos \phi_{j+1}}{4\Delta\phi} (u_{i+1j+1}^n + u_{i-1j+1}^n)(v_{i+1j+1}^n + v_{i-1j+1}^n) \\
 & \left. - \frac{\cos \phi_{j-1}}{4\Delta\phi} (u_{i+1j-1}^n + u_{i-1j-1}^n)(v_{i+1j-1}^n + v_{i-1j-1}^n) \right] \\
 & - \frac{2gh_{ij} \Delta t}{a\Delta\lambda \cos \phi_j} (\xi_{i+1j}^n - \xi_{i-1j}^n) + 4\Omega\Delta t v_{ij}^n \sin \phi_j \\
 & + 2S\Delta t u_{ij}^n v_{ij}^n a^{-1} \tan \phi_j + \frac{2\Delta t}{\rho_0} (\tau_\lambda)_n \\
 & + \frac{2\Delta t A}{a^2 \cos \phi_j} \left[ \frac{2}{(\Delta\lambda)^2 \cos \phi_j} (u_{i+1j+1}^{n-1} + u_{i+1j-1}^{n-1} + u_{i-1j+1}^{n-1} + \right.
 \end{aligned}$$



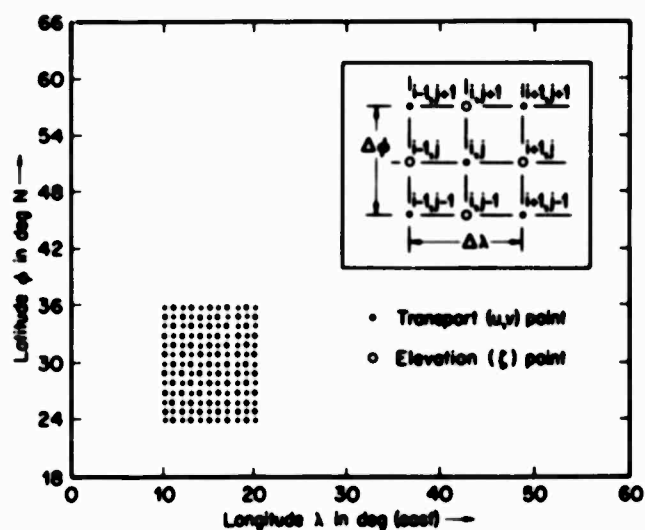


Fig. 1. A portion of the spherical finite-difference grid in the reference case  $\Delta\phi = \Delta\lambda = 2^\circ$ , showing the density of grid points on the same scale as subsequent figures. Here the longitude ( $\lambda$ ) and latitude ( $\phi$ ) of a grid point (relative to the origin  $\lambda = 0, \phi = \phi_0$ ) is given by  $\lambda = (i - 1)\Delta\lambda/2$  and  $\phi = \phi_0 + (j - 1)\Delta\phi/2$ , with  $i = 1, 2, \dots, 61, j = 1, 2, \dots, 49$ . The inset shows the structure of the interlocking transport (u,v) and elevation ( $\xi$ ) points.

$$\begin{aligned}
 & + u_{i-1j-1}^{n-1} - 4u_{ij}^{n-1} + \left( \frac{\cos \phi_j + \cos \phi_{j+1}}{(\Delta \phi)^2} \right) (u_{i+1j+1}^{n-1} + u_{i-1j+1}^{n-1} - 2u_{ij}^{n-1}) \\
 & + \left( \frac{\cos \phi_j + \cos \phi_{j-1}}{(\Delta \phi)^2} \right) (u_{i+1j-1}^{n-1} + u_{i-1j-1}^{n-1} - 2u_{ij}^{n-1}) + u_{ij}^{n-1} \quad (22)
 \end{aligned}$$

$$\begin{aligned}
 v_{ij}^{n+1} = & - \frac{2S\Delta t}{a \cos \phi_j} \left[ \frac{1}{4\Delta \lambda} (u_{i+1j+1}^n + u_{i+1j-1}^n) (v_{i+1j+1}^n + v_{i+1j-1}^n) \right. \\
 & - \frac{1}{4\Delta \lambda} (u_{i-1j+1}^n + u_{i-1j-1}^n) (v_{i-1j+1}^n + v_{i-1j-1}^n) \\
 & + \frac{\cos \phi_{j+1}}{4\Delta \phi} (v_{i+1j+1}^n + v_{i-1j+1}^n)^2 - \frac{\cos \phi_{j-1}}{4\Delta \phi} (v_{i+1j-1}^n + v_{i-1j-1}^n)^2 \Big] \\
 & - \frac{2gh_{ij}\Delta t}{a\Delta \phi} (\xi_{ij+1}^n - \xi_{ij-1}^n) - 4\Omega \Delta t u_{ij}^n \sin \phi_j \\
 & - 2S\Delta t (u_{ij}^n)^2 a^{-1} \tan \phi_j + \frac{2\Delta t}{\rho_o} (\tau_\phi^w)_{ij}^n \\
 & + \frac{2\Delta t A}{a^2 \cos \phi_j} \left[ \frac{2}{(\Delta \lambda)^2 \cos \phi_j} (v_{i+1j+1}^{n-1} + v_{i+1j-1}^{n-1} + v_{i-1j+1}^{n-1} \right. \\
 & + v_{i-1j-1}^{n-1} - 4v_{ij}^{n-1}) + \left( \frac{\cos \phi_j + \cos \phi_{j+1}}{(\Delta \phi)^2} \right) (v_{i+1j+1}^{n-1} + v_{i-1j+1}^{n-1} - 2v_{ij}^{n-1}) \\
 & + \left( \frac{\cos \phi_j + \cos \phi_{j-1}}{(\Delta \phi)^2} \right) (v_{i+1j-1}^{n-1} + v_{i-1j-1}^{n-1} - 2v_{ij}^{n-1}) \Big] + v_{ij}^{n-1} \quad (23)
 \end{aligned}$$

$$\begin{aligned} \xi_{ij}^{n+1} = & - \frac{2\Delta t}{e \cos \phi_j} \left[ \frac{1}{\Delta \lambda} (u_{i+1j}^n - u_{i-1j}^n) \right. \\ & \left. + \frac{1}{\Delta \phi} (v_{ij+1}^n \cos \phi_{j+1} - v_{ij-1}^n \cos \phi_{j-1}) \right] + \xi_{ij}^{n-1} \end{aligned} \quad (24)$$

Here, for example, the vertically integrated speed  $u_{ij}^n = u(i\Delta\lambda/2, j\Delta\phi/2, n\Delta t)$ , and similarly for  $v_{ij}^n$  and  $\xi_{ij}^n$ , where  $n = 1, 2, \dots$  and  $\Delta t$  is the time step size. At the initial time (corresponding to  $n = 0$ ), a single forward time step over  $\Delta t/2$  is taken, and all variables referenced at  $(n - 1)$  in (22) to (24) are replaced by the corresponding variables at  $n (= 0)$ . In the nonlinear terms of (22) and (23) the notation

$$U_{ij}^n = u_{ij}^n (h_{ij})^{-1/2}, \quad V_{ij}^n = v_{ij}^n (h_{ij})^{-1/2} \quad (25)$$

has been introduced for convenience, since the water depth is needed only at those points for which the (vertically integrated) speeds  $u$  and  $v$  are known. The frictional terms in  $A$  have been evaluated from the four corner or diagonal points with respect to  $ij$  and at the "backward" time step  $(n - 1)$  in order to achieve linear computational stability with the leapfrog differencing scheme, and the advective terms in  $S$  have been approximated in such a way to avoid nonlinear computational instability (Arikawa, 1966). We may note that in this scheme no explicit smoothing or interpolation is introduced.

Since (22) and (23) are to be applied only at points for which  $(i + j)$  is odd, while (24) applies only to points for which  $(i + j)$  is even, the necessary variables are automatically provided at the required grid points. A scheme in which all three variables are determined at each grid point would provide solutions no more accurate than those from the present procedure (for the same  $\Delta\lambda$ ,  $\Delta\phi$ , and  $\Delta t$ ). On the other hand, a scheme in which  $u$  is determined only at points for which  $i$  is odd and  $j$  is even, and  $v$  determined at points for which  $i$  is even and  $j$  is odd, would be a more economical scheme of comparable accuracy. There is some tendency, in fact, for the present solutions to split into two such partial solutions, although in general it makes little difference which set is selected.

In all of the present solutions the ocean basin is rectangular and of uniform depth, but in order to accommodate later studies of variable depth (and irregular shape) the system (22) to (24) has not been rewritten. A further assumption in the present work (with one exception noted later) is the prescription of a purely zonal wind stress

$$\begin{aligned}\tau_{\lambda}^w &= -T \cos \left( \frac{3\pi(j-1)}{2(J-1)} \right) \\ \tau_{\phi}^w &= 0\end{aligned}\tag{26}$$

where  $T = 2 \text{ dynes cm}^{-2}$  and where  $j = J$  denotes the northern wall of the basin.

The computational boundary conditions on the basin's edges may be written as

$$u_B^n = v_B^n = 0\tag{27}$$

for all  $n$  and for all boundaries (where  $B$  denotes boundary points for which  $i = 1, I$  or  $j = 1, J$ ), and

$$\xi_{1j}^{n+1} = \xi_{1j}^{n-1} - \frac{4\Delta t}{a\Delta\lambda \cos \phi_j} u_{2j}^n\tag{28a}$$

$$\xi_{Ij}^{n+1} = \xi_{Ij}^{n-1} + \frac{4\Delta t}{a\Delta\lambda \cos \phi_j} u_{I-1j}^n\tag{28b}$$

$$\xi_{11}^{n+1} = \xi_{11}^{n-1} - \frac{4\Delta t \cos \phi_{j+1}}{a\Delta\phi \cos \phi_j} v_{12}^n\tag{28c}$$

$$\xi_{1J}^{n+1} = \xi_{1J}^{n-1} + \frac{4\Delta t \cos \phi_{j-1}}{a\Delta\phi \cos \phi_j} v_{1J-1}^n\tag{28d}$$

for  $n = 1, 2, \dots$ . Here (28a) to (28d) apply to the western, eastern, southern, and northern boundaries, respectively, and represent the application of the continuity equation, (24), at the boundary, with the centered space difference replaced by a one-sided difference between the boundary and the next interior point, together with the condition (27). At  $n = 0$  these relations are replaced by the corresponding forward time-difference expressions.

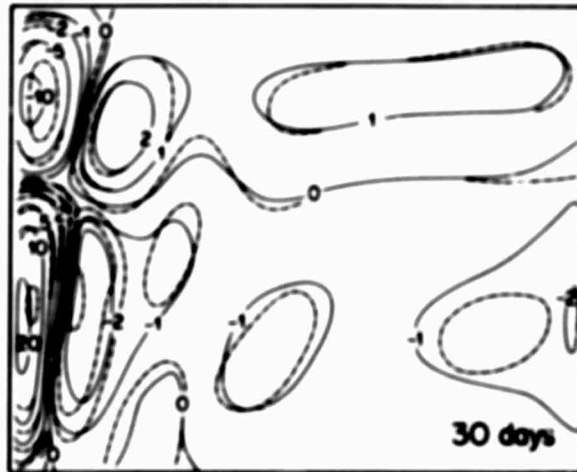
The fixed constants have been taken as  $a = 6371$  km,  $g = 980$  cm sec<sup>-2</sup>,  $\Omega = 7.292 \times 10^{-5}$  sec<sup>-1</sup>, and  $\rho_0 = 1$  g cm<sup>-3</sup>, while the remaining constants, fixed for any particular integration, are varied in a series of comparative solutions. A set of typical values (which specify a reference case) are  $A = 10^8$  cm<sup>2</sup> sec<sup>-1</sup>,  $S = 4/3$ ,  $\phi_0$  (southern boundary) = 18 N,  $\Delta\lambda = \Delta\phi = 2$  deg,  $\Delta t = 10$  min, and the basin's zonal and meridional widths  $(I - 1)\Delta\lambda/2$  and  $(J - 1)\Delta\phi/2$  given with  $I = 61$ ,  $J = 49$ . The integrations have proved stable when carried out for as long as 60 days of oceanic (simulated) time starting from an initially undisturbed ocean ( $u^0 = v^0 = \xi^0 = 0$ ), and require approximately 1 min of machine time per day of simulated time on the CDC 6600 computer.

#### IV. COMPARATIVE NUMERICAL SOLUTIONS--NUMERICAL AND GEOMETRICAL EFFECTS

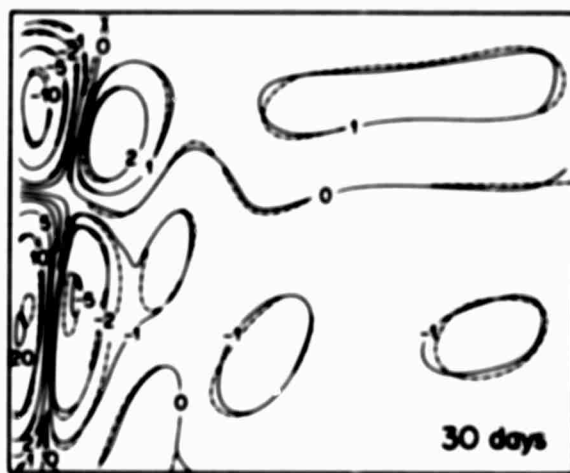
##### RESOLUTION TESTS

In a program of comparative numerical integration, one of the first questions to be examined should be the level of truncation error in the solutions. This is particularly important in the present problem in view of the narrowness of the western boundary currents and the characteristic presence of short planetary transient waves. We thus first examine the solutions' behavior as the resolution of the finite-difference grid is systematically changed, while all other parameters are held constant. For this purpose it is sufficeint to examine only the solutions for meridional transport, generated in the basin of fixed dimensions and subject to the steady wind stress, (26). This configuration will constitute a reference case, for which we select  $\Delta\lambda(I - 1)/2 = 60$  deg and  $\Delta\phi(J - 1)/2 = 48$  deg as the zonal and meridional dimensions of the basin,  $h = 400$  m,  $S = 4/3$ ,  $T = 2$  dyne  $\text{cm}^{-2}$ ,  $\phi_0 = 18$  N, and  $A = 2 \times 10^8$   $\text{cm}^2 \text{sec}^{-1}$ . Under these conditions the solutions of (22) to (24) for the meridional transport  $v$  at 30 days are shown in Fig. 2 for  $\Delta\phi(=\Delta\lambda) = 3^\circ$  and  $2^\circ$ , and each is compared with the higher-resolution case  $\Delta\phi(=\Delta\lambda) = 3/2^\circ$ .

Although the general character of the (meridional) circulation is similar in the  $3^\circ$  and  $3/2^\circ$  cases (Fig 2a), the  $3^\circ$  solution shows a systematic eastward displacement (relative to the  $3/2^\circ$  case) of the western countercurrents and the mid-ocean transients. Since these features evolve as westward-propagating Rossby waves, we may interpret this difference as a phase truncation error. In the western boundary currents themselves, the  $3^\circ$  solution has overestimated the maximum of the northward current and similarly underestimated the southward current, as summarized in Table 1, and in addition has positioned the flow too close to the boundary. In the southeastern portion of the basin a spurious southward "boundary" current is also present in the  $3^\circ$  solution, and persists throughout the calculation. This feature is apparently related to the solution's overestimate of the northward flow in the western



(a)



(b)

**Fig. 2.** The solutions for meridional transport  $v$  in  $Sv (100 km)^{-1}$  in a spherical basin at 30 days for  $\Delta\phi(= \Delta\lambda) = 3^\circ$  (a) and  $\Delta\phi(= \Delta\lambda) = 2^\circ$  (b), compared with the solution for  $\Delta\phi(= \Delta\lambda) = 3/2^\circ$  shown by dashed lines in both (a) and (b). Here  $A = 2 \times 10^8 cm^2 sec^{-1}$ ,  $h = 400 m$ ; the basin is 60 deg wide and extends from 18 N to 66 N. The (vertically-averaged) current  $v/h$  may be found in  $cm sec^{-1}$  by multiplying the isolines by the factor  $5/2$ .

Table 1  
EFFECTS OF RESOLUTION ON THE BOUNDARY CURRENT<sup>a</sup>

Gyre	Grid Mesh Size $\Delta\lambda = \Delta\phi$ (deg)	Maximum Meridional Current $v/h$ (cm sec <sup>-1</sup> )		Total Western Boundary Current Transport <sup>b</sup> ( $10^6$ m <sup>3</sup> sec <sup>-1</sup> )
		Western Boundary Current	Countercurrent	
Northern	3	-30	9	-33
	2	-34	9	-35
	3/2	-35	9	-36
Southern	3	60	-12	52
	2	51	-13	50
	3/2	50	-14	50

<sup>a</sup>For the case of Fig. 2 ( $A = 2 \times 10^8$  cm<sup>2</sup> sec<sup>-1</sup>,  $h = 400$  m,  $S = 4/3$ ) at 30 days.

<sup>b</sup>Based upon linear interpolation between grid points across the stream from the western boundary at the latitude of maximum current.



part of the southern gyre (see Table 1), and contributes to the relatively high total basin kinetic energy of  $6.8 \times 10^{23}$  ergs, compared with  $4.0 \times 10^{23}$  ergs for the halved ( $3/2^\circ$ ) grid. In overall performance the  $3^\circ$  grid therefore does not provide sufficient resolution.

The comparison of the  $2^\circ$  and  $3/2^\circ$  solutions in Fig. 2b, on the other hand, shows somewhat better correspondence. There is little systematic phase difference evident, and the magnitudes of the stronger transports in the west are in much closer agreement than in Fig. 2a (see also Table 1). The truncation-induced anomalous current along the eastern shore is also absent with the  $2^\circ$  (and  $3/2^\circ$ ) grid, and the basin's total kinetic energy of  $4.1 \times 10^{23}$  ergs is in good agreement with that for the  $3/2^\circ$  case. On this evidence we may conclude that the  $2^\circ$  grid gives adequate resolution throughout the basin and represents an economic selection as a reference resolution in further comparative integrations. Use of a finer grid in the western part of the basin, however, would result in a slightly better resolution of the intense boundary currents [as recognized earlier by Bryan (1963)], although the bulk of the truncation error has been removed in passing from the  $3^\circ$  to the  $2^\circ$  grid.

We may use the data of Table 1 to estimate the absolute size of the solutions' truncation error on the assumption that it varies as the square of the spatial mesh size. Since the maximum currents in the west generally do not occur at coincident points of the several grids, the total or net transport in the western boundary current serves as a comparable measure of truncation error. The net northward boundary current transports in the southern and northern gyres from Table 1 are thus 20 Sv ( $\text{Sv} = 10^6 \text{ m}^3 \text{ sec}^{-1}$ ), 15 Sv, and 14 Sv for the  $3^\circ$ ,  $2^\circ$ , and  $3/2^\circ$  grid solutions. If these transports contain a truncation error proportional to  $(\Delta\phi)^2$  superposed upon the true or truncation-free value, then the ratio  $(N_3 - N_2)(N_3 - N_{3/2})^{-1}$ , for example, should equal 20/27, where  $N_{\Delta\phi}$  is the net northward boundary current transport in the  $\Delta\phi$  grid solution. With the above values this ratio is 5/6, which may be taken as reasonable confirmation of the truncation hypothesis. If  $N_0$  denotes the truncation-free solution, then a percentage truncation error may be expressed by  $(N_{\Delta\phi} - N_0)N_0^{-1}$ , for example, giving a 25 percent error for

the 2° solution for the western boundary current (when the value  $M_0 = 12$  Sv as determined by the 3° and 3/2° grids is used). This is a maximum error for the 2° grid, as the transport of the longer reflected transient waves in the interior (see Fig. 2) are determined with somewhat greater accuracy.

#### SPHERICAL VERSUS 8-PLANE COORDINATES

In view of the widespread use of the 8-plane approximation in oceanic modeling, it is of interest to compare such solutions with those from the present spherical formulation. The 8-plane dynamical equations may be obtained from the system (19) to (21) by replacing  $\cos \phi$  by unity throughout, neglecting the terms in  $\tan \phi$ , and writing  $dx = a d\lambda$ ,  $dy = a d\phi$ . The resulting equations are:

$$\begin{aligned} \frac{\partial u}{\partial t} = & -S \left[ \frac{\partial}{\partial x} \left( \frac{u^2}{h} \right) + \frac{\partial}{\partial y} \left( \frac{uv}{h} \right) \right] - gh \frac{\partial \xi}{\partial x} \\ & + fv + \frac{1}{\rho_0} (\tau_x^u - \tau_x^b) + \Lambda \nabla^2 u \end{aligned} \quad (29)$$

$$\begin{aligned} \frac{\partial v}{\partial t} = & -S \left[ \frac{\partial}{\partial x} \left( \frac{uv}{h} \right) + \frac{\partial}{\partial y} \left( \frac{v^2}{h} \right) \right] - gh \frac{\partial \xi}{\partial y} \\ & - fu + \frac{1}{\rho_0} (\tau_y^u - \tau_y^b) + \Lambda \nabla^2 v \end{aligned} \quad (30)$$

$$\frac{\partial \xi}{\partial t} = - \frac{\partial u}{\partial x} - \frac{\partial v}{\partial y} \quad (31)$$

where  $u$  and  $v$  continue to be the vertically integrated volume transports  $\langle u \rangle$  and  $\langle v \rangle$ , and  $\nabla^2$  is the Laplacian in the rectangular coordinates  $x$  and  $y$ . Here the Coriolis parameter is now given by  $f = f_0 + \beta y$ , with  $f_0$  and  $\beta$  taken as constants. For a uniform-depth basin (and with  $S = 1$ ) this system is the same as that used in a previous study (Gates, 1968) when the meridional wind stress component and both components of the bottom

stress are neglected. This  $\beta$ -plane system may also be found by a formal transformation of the spherical equations, as shown, for example, by Varonia (1963), and is valid for the quasi-horizontal motions in a shallow ocean. The difference equations for the  $\beta$ -plane case may be readily written by appropriate simplification of the spherical equations, (22) to (24), and the  $\xi$ -boundary condition (28).

In the present application we continue to ignore the bottom stress, and select the constants  $\lambda = 10^8 \text{ cm}^2 \text{ sec}^{-1}$ ,  $h = 400 \text{ m}$ ,  $S = 4/3$ ,  $I = 61$ , and  $J = 49$  for both the  $\beta$ -plane and spherical cases, with the wind stress given by (26). For a reference solution on the sphere we select  $\Delta\lambda = \Delta\phi = 2^\circ$  and  $\phi_0 = 18 \text{ N}$ ; for the comparative solutions on the  $\beta$ -plane we select  $\Delta x = \Delta y = 222 \text{ km}$ ,  $f_0 = 4.507 \times 10^{-5} \text{ sec}^{-1}$ , and  $\beta = 1.701 \times 10^{-13} \text{ cm}^{-1} \text{ sec}^{-1}$ , the latter corresponding to the basin's average latitude,  $42 \text{ N}$ . These comparative solutions are shown in Figs. 3 and 4, and serve at the same time to document the time-dependent behavior in the spherical case.

The evolution of the meridional transport,  $v$ , shown in Fig. 3 (solid lines) consists of a series of transient Rossby waves reflected from the western shore, with these waves undergoing progressive slowing, shortening, and amplitude decay as they merge with the quasi-steady boundary currents. These transients are particularly prominent in the southern gyre, where they display a characteristic wavelength of some 15 to 20 deg (longitude), and move westward at speeds of approximately  $1.2 \text{ deg longitude day}^{-1}$  (about  $1.3 \text{ m sec}^{-1}$  at the gyre's center,  $34 \text{ N}$ ). While the western boundary current is in apparent equilibrium before the 21st day, the countercurrent offshore in the southern gyre responds to the periodic arrival and absorption of the transients; the southward transport in the west-central basin at 21 days, for example, may be seen merging with the southern gyre's countercurrent at 30 days, while a succeeding transient now occupies the former's offshore position. It also appears that by 48 days these transients have undergone reflection from the southern boundary of the basin (Gates, 1969). In the northern gyre the (northward) countercurrent is in position after about 30 days, and shows little subsequent change. The transient Rossby waves in this gyre are also seen to move slowly to the west (averaging

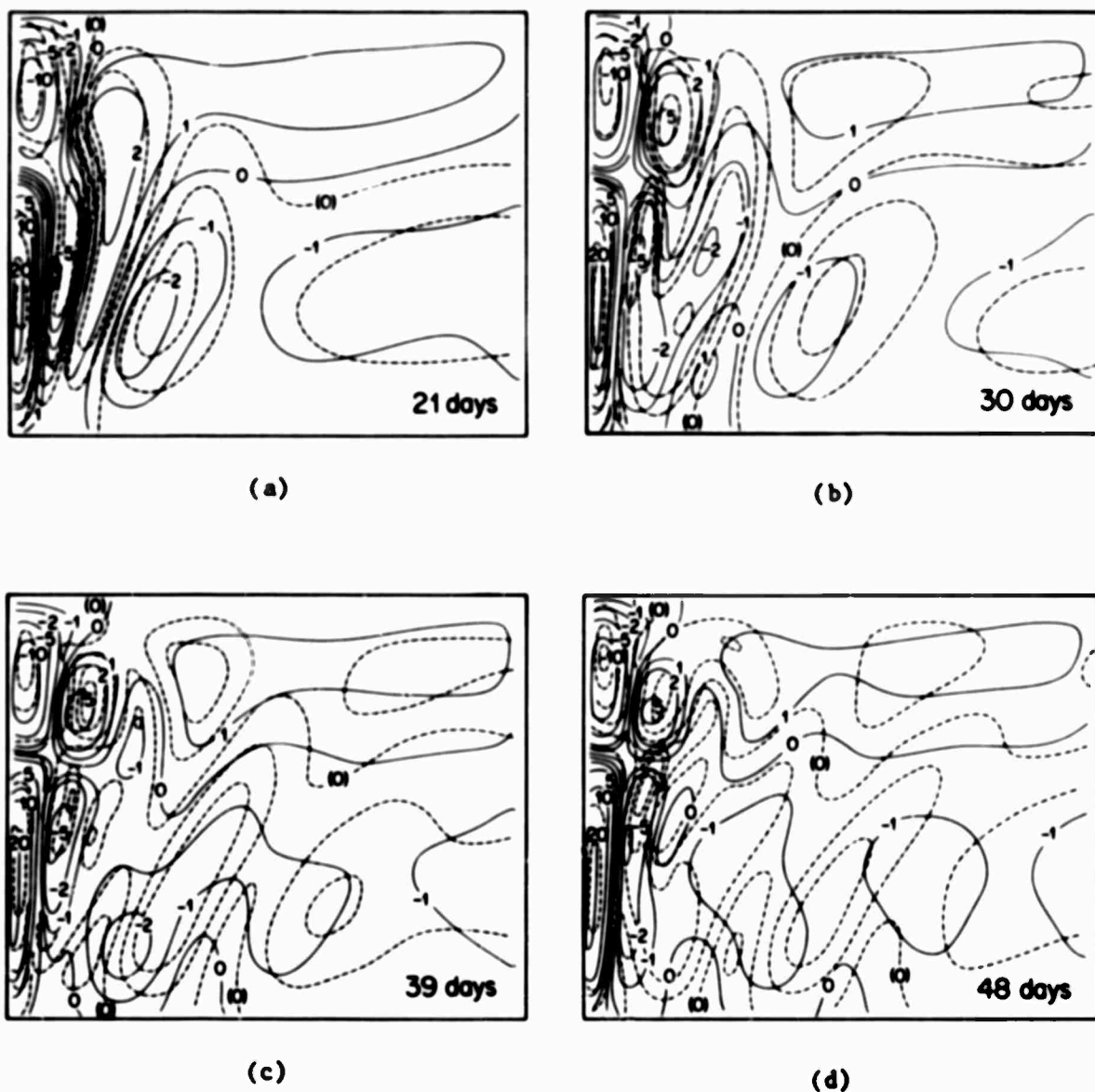


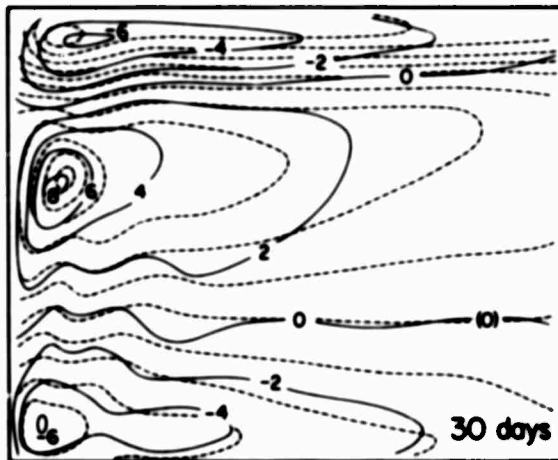
Fig. 3. The solutions for meridional transport  $v$  in  $\text{Sv } (100 \text{ km})^{-1}$  in a spherical basin with  $\Delta\lambda = \Delta\phi = 2^\circ$  (solid lines) and in a  $\beta$ -plane with  $\Delta x = \Delta y = 222 \text{ km}$  (dashed lines). Here  $A = 10^8 \text{ cm}^2 \text{ sec}^{-1}$ ,  $h = 400 \text{ m}$  and the basin extends from  $18^\circ \text{ N}$  to  $66^\circ \text{ N}$ . The same isoline spacing (uneven) has been used for both the spherical and  $\beta$ -plane solutions, with only the zero isoline labeled (in parentheses) in the latter case. The  $\beta$ -plane solutions have been spaced eastward from the western boundary according to  $\sec \phi$  to approximate the geometry of the spherical solutions. The mean current  $v/h$  in  $\text{cm sec}^{-1}$  is given by multiplying the transport isolines by factor  $5/2$ .

about  $0.4 \text{ deg longitude day}^{-1}$ ), and are less well developed than their counterparts in the southern gyre. These same general features are also reflected in the solutions for the zonal transport,  $u$ , and surface elevation,  $\zeta$ , shown in Fig. 4 at 30 days, although the role of the transients is less conspicuous in these variables.

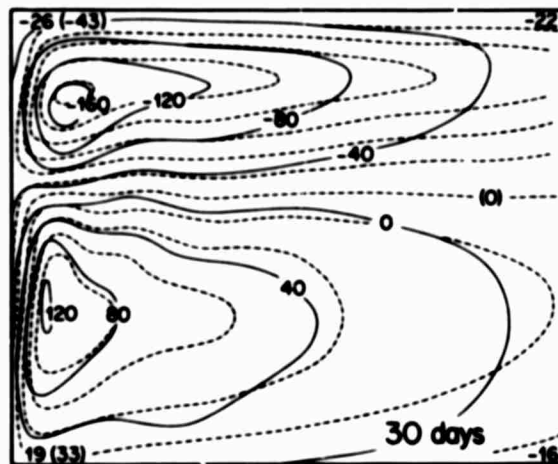
Of particular interest are the comparative solutions for the  $\beta$ -plane also shown in Figs. 3 and 4 (dashed lines). Here the northward finite-difference mesh size is the same in the spherical and  $\beta$ -plane solutions ( $2^\circ$ ), while the eastward mesh size is different at each latitude over the basin ( $2^\circ$  longitude compared with 222 km). Starting with points coincident with the spherical grid on the western boundary, the solutions on the  $\beta$ -plane have here been plotted with the points at each latitude,  $\phi$ , displaced eastward according to  $2^\circ \sec \phi$ , in order to remove the zonal scale distortion of the spherical geometry. The eastern portion of the  $\beta$ -plane grid is therefore not seen in these figures, and the two solutions should not be compared in the eastern third or so of the (60-deg) grid shown.

In the western and central portions of the basin, we see a close correspondence in the general patterns of the two solutions, although there are two significant differences. In the southern gyre the transients of the  $\beta$ -plane solution lie systematically to the east of their spherical counterparts. This displacement, moreover, is cumulative with time, and indicates that the westward phase speed of the  $\beta$ -plane transients is approximately 90 percent of that in the spherical solutions. This effect is evidently not due to the differences in zonal truncation error in the two solutions, as the phase differences are smaller in the northern gyre where the solutions' zonal mesh discrepancy is the greatest. A second systematic difference is a northward displacement of the  $\beta$ -plane solutions of about  $2 \text{ deg}$  relative to the spherical case. This effect is present over most of the basin and persists throughout the calculation, and may be related to the choice of the constants  $f_0$  and  $\beta$ .

Even a cursory examination of Figs. 3 and 4, however, shows that the greatest difference between the spherical and  $\beta$ -plane solutions is the somewhat larger amplitude of the transports (and water elevation) in the  $\beta$ -plane case: in general this excess amounts to about 50 percent



(a)



(b)

Fig. 4. The solutions for zonal transport  $u$  in  $\text{Sv} (100 \text{ km})^{-1}$  (a) and for water elevation  $\xi$  in cm (b), accompanying the solutions of Fig. 3 at 30 days. The dashed lines are the solutions on the  $\beta$ -plane (see Fig. 3).

of the spherical case's amplitudes. More detailed data on these differences are given in Table 2 for the important western boundary current, which we note to be generally stronger and slightly narrower in the  $\beta$ -plane case. Since the boundary conditions, basin depth, lateral viscosity, meridional grid size, and the imposed wind stress are the same in both solutions, the source of this difference is to be found in the geometry of the  $\beta$ -plane approximation itself; namely, the progressive narrowing with latitude of the basin's zonal width in the spherical formulation with meridional boundaries. Although the meridional dimensions of the two basins are the same, the zonal dimensions differ by more than a factor of two at the northern boundary. With a Sverdrup equilibrium over the interior of the basin, the integral of the wind-stress curl is proportional to the total interior meridional flow, and hence, through continuity, is a measure of the net flow in the western boundary currents. In the present cases, the ratio of the area integral of the curl of the wind stress for the spherical and  $\beta$ -plane basins is 0.42, and the ratio of the net northward transport in the western boundary currents in the two cases is 0.48 from the data of Table 2. This agreement would be even closer were the western countercurrents' transport also considered. The magnitude differences in the solutions of Figs. 3 and 4 are thus believed to be due to this areal effect, and close quantitative agreement could be expected if the eastern boundary in the  $\beta$ -plane basin were moved progressively westward with latitude in order to approximate the zonal dimension of the spherical basin.

In theoretical studies of the adequacy of the  $\beta$ -plane approximation in a nonviscous model, Longuet-Higgins (1964, 1965) has shown that the periods of at least the lower-order modes (of free oscillations) in simple enclosed basins of modest size should agree to within about 10 percent in the spherical and  $\beta$ -plane solutions. This conclusion is supported by the transient behavior discussed above in connection with Fig. 3. From analytical solutions for a linear, nondivergent model with bottom friction, Takano (1966) has also shown that the principal difference between (steady) spherical and  $\beta$ -plane solutions is the increased boundary current transport of the latter at higher latitudes, due to the increased basin width of the  $\beta$ -plane formulation. This is

Table 2  
CHARACTERISTICS OF WESTERN BOUNDARY CURRENT IN SPHERICAL AND  $\beta$ -PLANE SOLUTIONS

Gyre	Time (days)	Maximum Current (cm sec <sup>-1</sup> )		Latitude (N) of Maximum		Zonal Width at Maximum (km)		Total Transport <sup>a</sup> (Sv = 10 <sup>6</sup> m <sup>3</sup> sec <sup>-1</sup> )	
		Sphere	$\beta$ -plane	Sphere	$\beta$ -plane	Sphere	$\beta$ -plane	Sphere	$\beta$ -plane
Northern	21	-35	-47	56	58	430	485	-38	-44
	30	-42	-67	56	58	390	365	-41	-46
	39	-41	-73	56	58	365	345	-38	-49
	48	-40	-76	56	60	370	330	-37	-50
	57 <sup>b</sup>	-40	-78	56	60	370	325	-37	-51
Southern	21	68	105	32	32	400	320	49	67
	30	72	120	32	34	390	340	50	80
	39	69	117	32	34	405	320	50	75
	48	70	118	32	34	400	330	51	78
	57 <sup>b</sup>	71	120	32	34	400	330	51	80

<sup>a</sup>Based upon linear interpolation between grid points across the stream from the western boundary at the latitude of maximum current.

<sup>b</sup>Solutions not shown in Fig. 3.



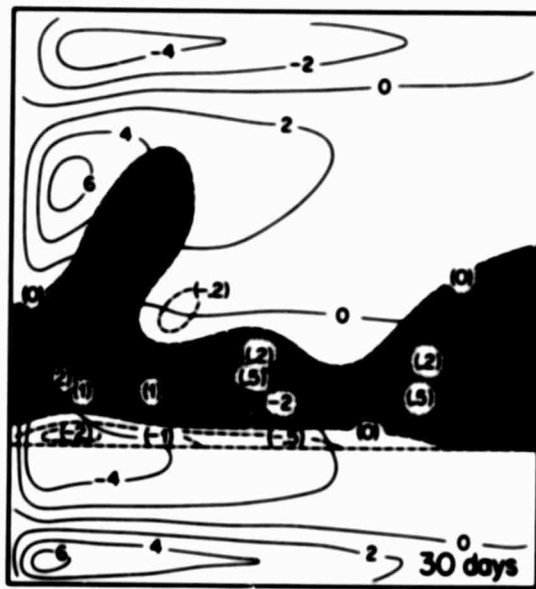
confirmed by the present solutions, which may therefore be taken as a demonstration of the adequacy of the  $\beta$ -plane approximation for the time-dependent motions in the lower and middle latitudes. In the numerical simulation of realistic oceanic motions, however, there seems to be no reason not to employ the more general spheroidal system, and it will be used in the further comparative solutions discussed below.

#### EFFECTS OF THE BOUNDARY AND BASIN SIZE

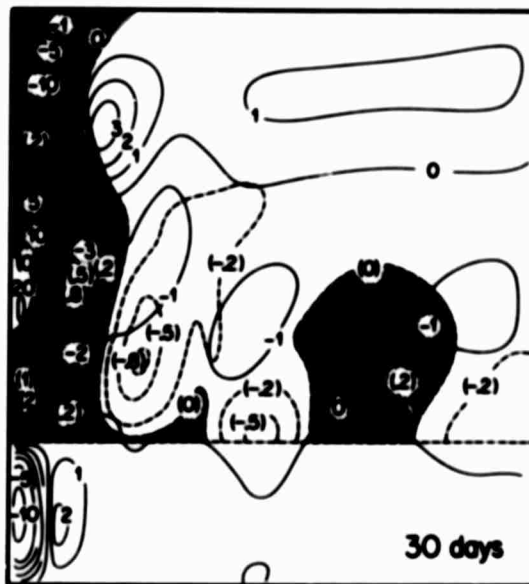
In a wind-driven oceanic model the location of the regions of zonal inflow and outflow to the western boundary current is determined both by the spatial variation of the imposed wind stress and by the location of the zonal boundaries of the basin. In an effort to document this latter, geometrical effect as distinguished from the former, dynamical one, a comparative integration was made in which the southern boundary was moved farther south, as well as a second integration in which the basin's zonal width was reduced. The same zonal wind-stress pattern was used in each case, with the solutions of a (spherical) case of intermediate basin size serving as a reference.

With the constants  $A = 2 \times 10^8 \text{ cm}^2 \text{ sec}^{-1}$ ,  $\Delta\lambda = \Delta\phi = 2^\circ$ ,  $h = 400 \text{ m}$  and  $S = 4/3$ , the solutions for the transports at 30 days are shown in Fig. 5 for the comparative basins of 48 deg and 64 deg latitudinal extent. The wind stress is given by (26) for the 48-deg case, and by  $\tau_\lambda^W = -T \sin [2\pi(j-1)(J-1)^{-1}]$ ,  $\tau_\phi^W = 0$  for the 64-deg case (with  $j = 1$  now at 2 N) to ensure coincidence of the stress in the region common to both basins. (In all cases  $T = 2 \text{ dynes cm}^{-2}$ .) The imposition of the southern boundary at 18 N results in a decrease of the westward and northward transports near the southern and western boundaries, respectively, as shown by the dashed lines in Fig. 5. Beyond this boundary zone of some 2 to 4 deg width, the presence of the southern boundary at 18 N produces an increased westward transport relative to the 2 N case in a broad zonal band extending approximately half way across the basin.

The differences in the meridional transport, also shown in Fig. 5, are similarly confined to the southern and western regions of the basin. Imposition of the southern boundary at 18 N (rather than at 2 N) has generally limited the southward transport in the interior of the basin,



(a)

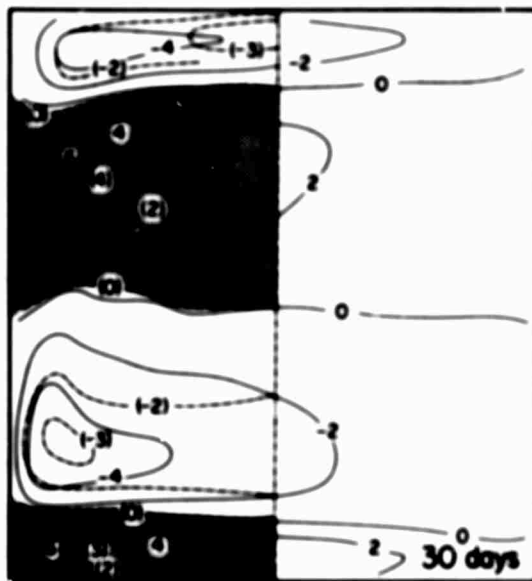


(b)

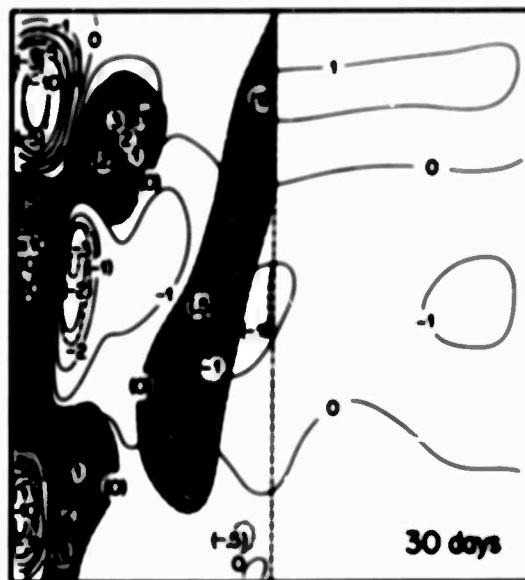
Fig. 5. The solutions for zonal transport (a) and meridional transport (b) in  $Sv(100\text{ km})^{-1}$  at 30 days with the southern boundary removed to 2 N. Here  $\Delta\lambda = \Delta\phi = 2^\circ$ ,  $A = 2 \times 10^8\text{ cm}^2\text{ sec}^{-1}$ , and  $h = 400\text{ m}$ . The differences with respect to corresponding solutions with the southern boundary at 18 N are shown by the dashed lines (2 N case minus 18 N case). The (vertically-averaged) currents  $u/h$  and  $v/h$  in  $\text{cm sec}^{-1}$  are given by multiplying the transport isolines by the factor 5/2.

end limited the northward transport in nearly all of the western boundary current system. The largest boundary effects on both the zonal and meridional transport are thus found where the flow is the most intense, which indicates that the effect of a particular boundary is very much dependent upon its location with respect to circulation inferred from the driving stress pattern. The 18° N boundary in Fig. 5 is at a latitude of small meridional transport but large zonal transport in the 2° N solution; were the boundary at 34° N, for example, less effect on the zonal flow but more effect on the meridional flow could be expected. In the southern interior of the 18° N basin the boundary-induced transport changes are of the order of 25 to 50 percent of the solutions with a more distant southern boundary, and this effect should be kept in mind when interpreting near-boundary circulations. A similar sensitivity to relocation of the northern boundary could also be expected in the present cases.

In a subsequent experiment the location of the eastern boundary was changed from that in Fig. 5 to a position in the center of this basin. The transport changes produced at 30 days by this alteration are shown in Fig. 6, again referenced to the larger (60-deg long) basin's solutions. The contribution of the eastern half-basin is seen to be responsible for approximately half of the maximum transports in the western ocean. In particular, the meridional western boundary currents are present on the same scale in both solutions, and are very nearly halved in speed by the halving of the basin's east-west dimension, while the maximum zonal transport is reduced by approximately 60 percent. Since the same zonal wind-stress distribution was imposed in both cases, these transport changes are the direct result of the basin's changed width. The interior meridional flow is little affected by the width changes, and the net meridional transport accumulates with distance from the eastern boundary as shown by Sverdrup (1947). The intensity (but not the scale) of the western boundary current is then determined by the continuity requirement to balance this flow. The total kinetic energy in the 30- and 60-deg longitude basins at 30 days is  $1.0 \times 10^{23}$  ergs and  $5.6 \times 10^{23}$  ergs, respectively, and is a further reflection of the approximate halving of the larger transports. This



(a)



(b)

**Fig. 6.** The solutions for zonal transport (a) and meridional transport (b) in  $Sv$   $(100\ km)^{-1}$  at 30 days, with the dashed lines indicating the difference in transport with the eastern boundary at 30 deg longitude rather than at 60 deg longitude (30 deg case minus 60 deg case). Here  $A = 2 \times 10^8\ cm^2\ sec^{-1}$ ,  $h = 400\ m$ , and  $\Delta\lambda = \Delta\phi = 2^\circ$  as in Fig. 5. The average currents in  $cm\ sec^{-1}$  are given by multiplying the transport isolines by the factor  $5/2$ .

same effect was previously identified as the likely cause of the systematic magnitude differences between the otherwise comparable solutions on the sphere and S-plane in Figs. 3 and 4.

The boundary-induced circulation changes discussed above should not be regarded as "errors" in any sense, but rather as indications of the sensitivity of the solutions to the actual placement of the basin's lateral boundaries. As applied to the world's oceans, these results would suggest that the vertically-integrated transport of the western boundary currents in the Pacific ocean, for example, should be approximately double those in the Atlantic, in view of the two oceans' approximate 2 to 1 zonal dimension ratio and their generally comparable stress fields. The fact that the Kuroshio's transport is generally less than that of the Gulf Stream may be due to the presence of a large baroclinic component in the latter's transport, or to other factors not considered in the present wind-driven homogeneous model.

## V. COMPARATIVE NUMERICAL SOLUTIONS--PHYSICAL EFFECTS

### FRICTIONAL EFFECTS

Although the wind-driven circulation in the interior of an ocean basin is generally characterized by a Sverdrup equilibrium (approximate balance between the local wind-stress curl and the planetary vorticity ( $\beta$ ) tendency), the western boundary currents are known to be critically influenced by frictional forces. While the boundary currents may not owe their existence in a fundamental sense to the friction (when we view such currents as the result of the trapping of westward propagating Rossby waves), their width and intensity are principally determined by viscous effects if we assume that the nonlinear inertial effects are not dominant.

Since the work of Munk (1950) a lateral eddy viscosity  $A$  of the order  $10^7$  to  $10^8$   $\text{cm}^2 \text{sec}^{-1}$  in wind-driven models has provided reasonable values for the width and transport of the western boundary current, although actual boundary currents appear to be systematically narrower and more intense. The variation of such solutions to changes in the lateral viscosity has been documented by Bryan (1963) on the  $\beta$ -plane: a relatively large value of  $A$  will produce a smoothed and "sluggish" circulation, while a relatively small value will produce an intense and narrow boundary current which may become unstable. Presumably a similar behavior would occur in the present (spherical) formulation, and some data are given in Table 3; here solutions have not been accomplished for values of  $A$  less than  $6 \times 10^7$   $\text{cm}^2 \text{sec}^{-1}$  with the present 2-deg resolution. These data, as well as a comparison of Figs. 2 and 3, show that the intensity of the meridional current at 30 days is multiplied by a factor of approximately 0.7 by the doubling of  $A$  from  $10^8$   $\text{cm}^2 \text{sec}^{-1}$  to  $2 \times 10^8$   $\text{cm}^2 \text{sec}^{-1}$ . A closer inspection shows that the western boundary current in both the northern and southern gyres is approximately 10 percent wider in the case of the larger  $A$ . These results may be compared with the factors  $2^{-1/3}$  and  $2^{1/3}$  to be applied to the intensity and width, respectively, accompanying a doubling of  $A$  according to the theory of a (linear) viscous boundary layer

Table 3  
EFFECTS OF FRICTION ON THE WESTERN BOUNDARY CURRENT<sup>a</sup>

Lateral Friction, A ( $10^8 \text{ cm}^2 \text{ sec}^{-1}$ )	Bottom Friction, k ( $10^{-6} \text{ sec}^{-1}$ )	Time (days)	Maximum Current, v/h ( $\text{cm sec}^{-1}$ )	Zonal Width (km)	Total Transport <sup>b</sup> ( $Sv = 10^6 \text{ m}^3 \text{ sec}^{-1}$ )
1.0	0	30	72	390	48
		45	69	400	49
		60	70	395	48
1.0	1.0	30	50	440	42
		45	49	445	42
		60	49	445	42
2.0	0	30	51	425	48
		45	49	440	48
		60	50	440	48
2.0 <sup>c</sup>	0.5 <sup>c</sup>	30	43	460	44
		45	42	470	44
		60	42	470	44

<sup>a</sup>At 32N, with  $h = 400 \text{ m}$ ,  $\beta = 4/3$ .

<sup>b</sup>Based upon linear interpolation between grid points across the stream from the western boundary.

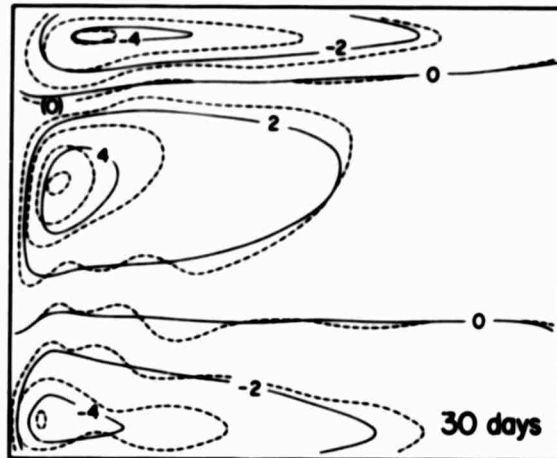
<sup>c</sup>Solutions not shown.

(Munk, 1950), whereas the current's total transport is independent of  $A$ . There is also a small (2-deg longitude) but systematic eastward displacement of the transients in the central ocean for the case of the larger  $A$ , as well as a slight amplitude reduction. In this respect the effect of increasing the lateral viscosity is similar to that produced by an increase in the grid-mesh size noted earlier in connection with Fig. 2.

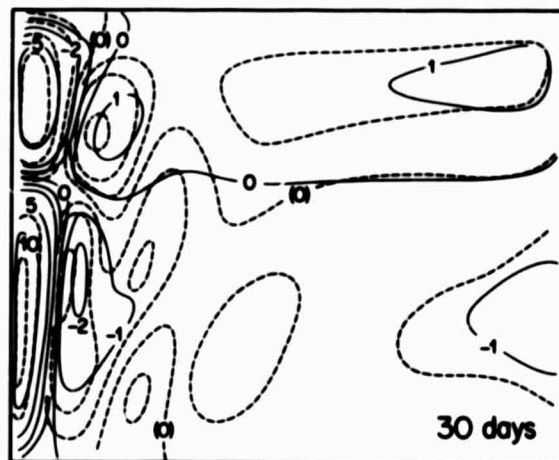
The viscous dissipation in a wind-driven homogeneous model may also be formulated in terms of an Ekman (or bottom) friction in the manner of Stommel (1948). Some evidence on the response of the near-equilibrium circulation of such an ocean to variations of the bottom friction coefficient has been given by Veronis (1966b, 1966c), but only for systems in which the nonlinear inertial terms were relatively more important. Since this model provides for no countercurrents and characteristically places the maximum meridional current at the western boundary itself, integrations have not been made with the replacement of lateral friction by bottom friction in the present formulation. Rather, the sensitivity of the present model with lateral viscosity to the addition of a bottom frictional dissipation has been considered. The results of such a comparative integration are shown in Fig. 7 for  $A = 10^8 \text{ cm}^2 \text{ sec}^{-1}$  and with the coefficient  $k = 10^{-6} \text{ sec}^{-1}$  in the added bottom frictional terms  $-ku$  and  $-kv$  on the right-hand sides of (19) and (20), respectively. (These terms were evaluated at the backward time level  $n - 1$  in the finite-difference equations (22) and (23) to promote computational stability.) Also shown as dashed lines in Fig. 7 are the comparative or reference solutions for the case of a lateral viscosity  $A = 10^8 \text{ cm}^2 \text{ sec}^{-1}$  alone.

The maximum zonal flow in the western part of the basin is seen to be reduced by the bottom friction to about 2/3 of its value with lateral friction alone, although the location and shape of the circulation patterns are similar. In the remainder of the basin the zonal flow (which is very nearly geostrophic) is affected very little by the introduction of bottom friction. This indicates that the north/south profile of the free water surface is maintained primarily by the meridional transport in the surface Ekman layer induced by the zonal wind





(a)



(b)

Fig. 7. The solutions for zonal transport (a) and meridional transport (b) in  $Sv (100 km)^{-1}$  at 30 days with a bottom friction coefficient  $k = 10^{-6} sec^{-1}$  and lateral viscosity  $A = 10^8 cm^2 sec^{-1}$  (solid lines). The corresponding solutions with lateral viscosity alone are shown by dashed lines. The mean currents  $u/h$  and  $v/h$  in  $cm sec^{-1}$  are given by multiplying the transport isolines by the factor  $5/2$  for the present 400 m basin.

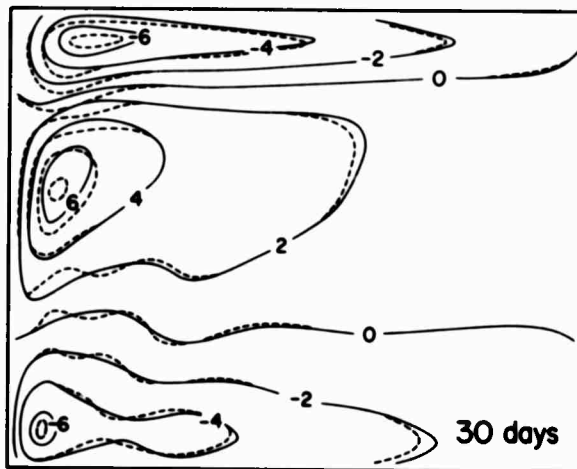
stress distribution. The maximum meridional current in Fig. 7 near the western boundary is also reduced to approximately two-thirds its value with lateral viscosity alone, while the current's width is increased by the introduction of bottom friction. From these solutions (and the data of Table 3) we deduce that the value  $k = 10^{-6} \text{ sec}^{-1}$  has approximately the same effect on the maximum meridional current as does a value of  $A$  of about  $10^8 \text{ cm}^2 \text{ sec}^{-1}$ . Bottom friction, however, reduces the total transport of the western boundary current, in contrast to the transport's independence of the lateral viscosity (with no bottom friction).

This dynamical equivalence applies only to the quasi-stationary boundary currents, however. We note from Fig. 7 that the transients prominent in the west-central ocean with only lateral viscosity have been almost completely damped out by the introduction of bottom friction. This illustrates the sensitivity of transient Rossby waves to this form of dissipation. If we interpret the magnitude of the lateral viscous term  $AV^2v$  for these transients in terms of a characteristic decay time  $t_l = v_m (AV^2v)^{-1}$ , where  $v_m$  is a typical transient's amplitude, we find  $t_l = 46$  days for the typical wave of 1600 km length when  $A = 10^8 \text{ cm}^2 \text{ sec}^{-1}$ . Since the period of these waves (about 14 days; see Fig. 3) is somewhat less than this decay time, we may expect a succession of (reflected) waves to appear in the west-central basin, with each wave less intense than its predecessor and gradually merging into the western boundary current system. The corresponding decay time with bottom friction is  $t_b = k^{-1}$ , or about 12 days with  $k = 10^{-6} \text{ sec}^{-1}$ . In this case the transient waves would be almost completely damped in a time less than their own period, and would effectively disappear from the solution. The relative prominence (or absence) of transient Rossby waves in the meridional flow in the western part of the oceans may therefore be indicative of the relative role of lateral and bottom friction, although a nonlinear viscosity may also be operative. A similar damping of transient motions by the introduction of bottom friction into a baroclinic oceanic model has been noted by Bryan and Cox (1968).

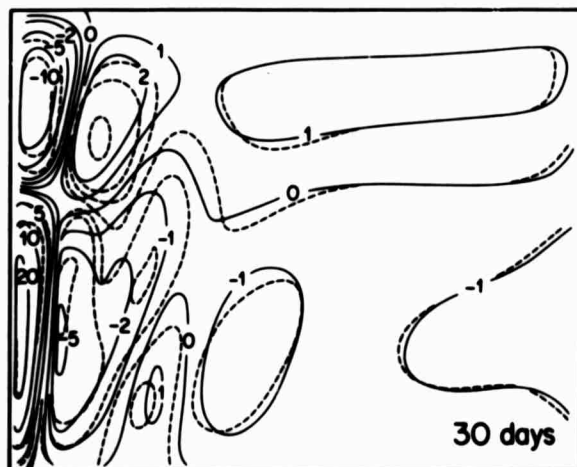
### NONLINEAR EFFECTS

It is of interest to document the role of nonlinear momentum advection in the present spherical model, and to this end a comparative integration was made with the omission of the inertial terms in (19) and (20) by the selection  $S = 0$ . The resulting solutions for the transport at 30 days are shown in Fig. 8, with the parameters  $\Delta\lambda = \Delta\phi = 2^\circ$ ,  $A = 10^8 \text{ cm}^2 \text{ sec}^{-1}$ ,  $h = 400 \text{ m}$ , and with the zonal stress (26) over the 60-deg longitude, 48-deg latitude basin as before. We see at once that the transport is similar in the linear and nonlinear solutions. The maximum eastward flow in mid-latitudes is slightly weaker in the linear version, but elsewhere the zonal transport solutions are almost indistinguishable. The maximum meridional boundary-current transports are likewise very nearly the same in both solutions, as is the interior transport pattern. Only the meridional countercurrents in the west are noticeably weaker in the linear version, and this effect is in accord with the results of Veronis (1966c) for the corresponding non-divergent  $\beta$ -plane model. The meridional transient motions seaward of these countercurrents are likewise weakened by the deletion of the nonlinear terms, and in general display less meridional tilt than their nonlinear counterparts. This effect was previously noted in the  $\beta$ -plane solutions discussed by Gates (1968), although it is apparently less marked in the present spherical formulation.

We note that the nonlinear solutions in Fig. 8 are for the value  $S = 4/3$ , which corresponds to a linear decrease of speed with depth toward zero at the ocean bottom. The solutions with this value do not differ significantly from those with  $S = 1$  (not shown), corresponding to a current uniform over depth, nor from those with  $S = 4$  (not shown), corresponding to a more nearly exponential (and possible more realistic) current profile. For the  $S = 4$  case the interior transient motions are slightly less intense than those shown in Fig. 8, although the overall similarity of the solutions is testimony to the relatively minor role played by the nonlinearity introduced by  $S$  of the order unity. This is in accord with the three-dimensional solutions of Bryan and Cox (1967) for a similarly modest degree of nonlinearity. The more highly nonlinear solutions reported by Bryan and Cox (1968) would appear to



(a)



(b)

**Fig. 8.** The linear solutions for zonal transport (a) and meridional transport (b) in  $Sv$  ( $100 \text{ km}^{-1}$ ) at 30 days with  $S = 0$  (solid lines), compared with the corresponding non-linear solutions with  $S = 4/3$  (dashed lines). Here  $A = 10^8 \text{ cm}^2 \text{ sec}^{-1}$  and  $h = 400 \text{ m}$ . The mean currents  $u/h$  and  $v/h$  in  $\text{cm sec}^{-1}$  are given by multiplying the transport iso-lines by the factor  $5/2$ .

correspond to values of  $S$  of the order of 10 to 100, and represent a marked confinement of the (wind-driven) transport to the surface layers. Integrations for this range of  $S$  have not been performed with the present model.

#### DEPTH EFFECTS

Since the ocean depth has been assumed constant in the present solutions, its value has been selected as representing in some way the upper oceanic region, wherein the wind-driven barotropic mode might be expected to be most evident. These solutions cannot be considered adequate simulations of the oceanic surface layer, however, in view of their neglect of the substantial variations of thermocline depth. Strictly speaking, we have here studied the behavior of only a shallow homogeneous sea, and it may therefore be of interest to examine the effect of the (uniform) depth selected for such a basin.

The comparative solutions for zonal and meridional transport shown in Fig. 9 display the effects of increasing the depth  $h$  from 400 m to 1200 m, with the values  $S = 4/3$  and  $A = 2 \times 10^8 \text{ cm}^2 \text{ sec}^{-1}$  common to both integrations. The solutions for zonal transport are only slightly altered by the depth increase, and the maximum meridional transports along the western boundary are also nearly the same in both solutions. This is in agreement with the numerical solutions of Bryan and Cox (1967), which show the mean wind-driven transport to be relatively insensitive to the basin's (uniform) depth provided it exceeds a characteristic scale depth. There are, however, noticeable differences in the position and strength of the transients, which are most clearly seen in the west-central basin in the meridional transport solutions of Fig. 9. These transients are Rossby waves reflected from the western boundary, and are propagating westward relative to the zonal current. The behavior of such waves is essentially described by the linear inviscid theory for the basin's free oscillations, as shown for example, by the numerical studies of Gates (1969). The primary effect of a depth increase on these waves would therefore be an increased (reflected) transient wavelength and an increased westward phase speed, both induced through the divergence permitted by the free-surface variations. The

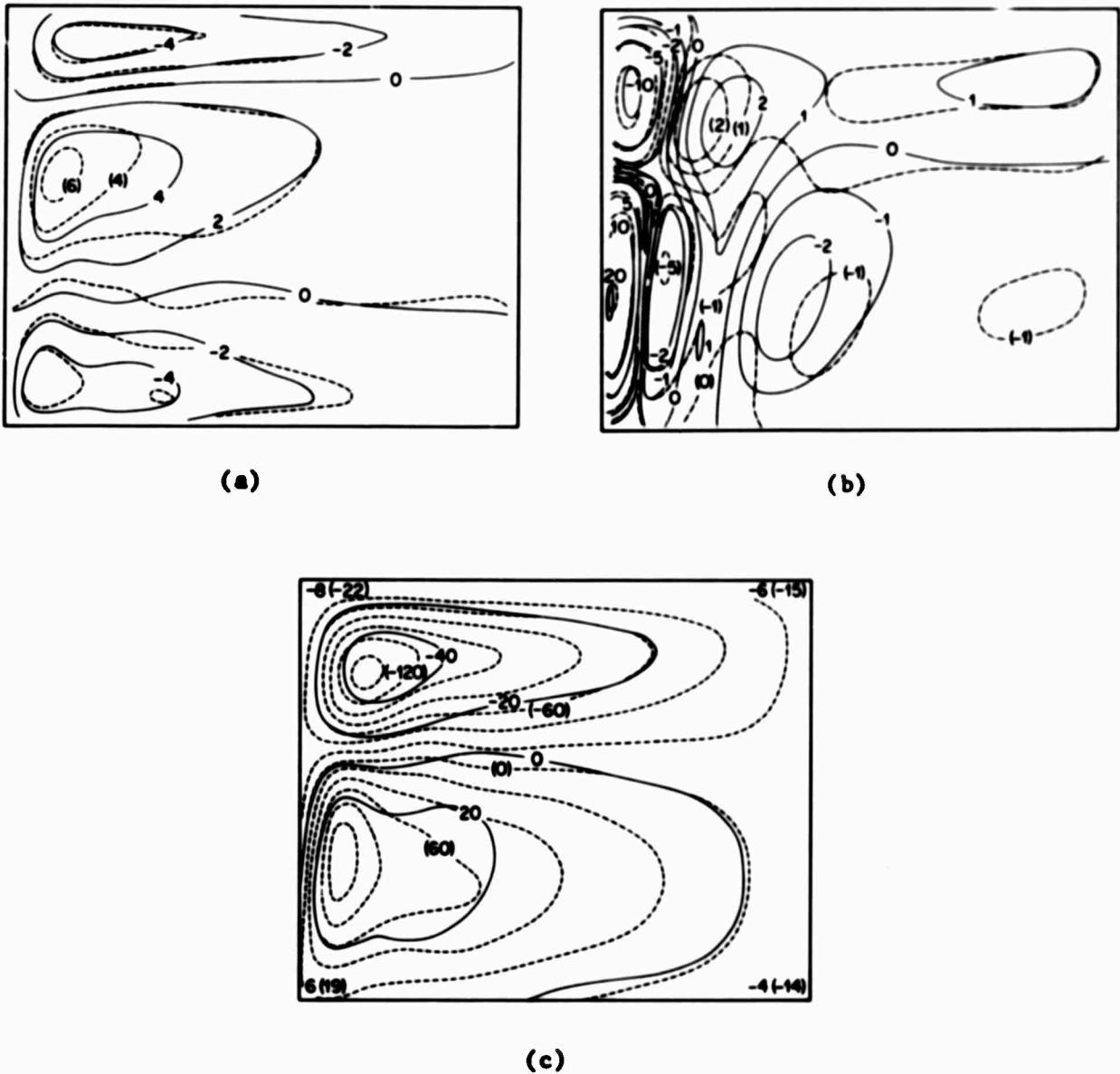


Fig. 9. The solutions for zonal transport (a) and meridional transport (b) in  $\text{Sv (100 km)}^{-1}$  at 30 days with the depth  $h = 1200 \text{ m}$  (solid lines) and  $h = 400 \text{ m}$  (dashed lines). The corresponding solutions for water elevation in cm are also shown (c), with the contours drawn every 20 cm in both cases. Here  $S = 4/3$  and  $A = 2 \times 10^8 \text{ cm}^2 \text{ sec}^{-1}$ . The mean currents  $u/h$  and  $v/h$  in  $\text{cm sec}^{-1}$  are given by multiplying the solid transport isolines by the factor  $5/6$  and the dashed isolines by the factor  $5/2$ .

phase differences between the transients in the south-central basin in Fig. 9 at 30 days, for example, are consistent with the phase speed increase (from  $1.3 \text{ m sec}^{-1}$  to  $1.5 \text{ m sec}^{-1}$ ) to be expected from the depth change from 400 m to 1200 m. The apparent increase in transient wavelength may also be accounted for by reflection from the western shore in the deepened basin.

We may speculate that changes in the transient's behavior similar to those in Fig. 9 would be produced if the basin's depth were increased by a further factor of three (from 1200 m to 3600 m), in order to approximate the average depth of the world's oceans. On the basis of the present evidence, however, no significant change would be expected in the transport or structure of the important western boundary currents. The present solutions thus provide justification for the continued use of a relatively shallow basin in studies of a barotropic ocean, at least in a program of comparative integrations for the wind-driven transport.

In terms of the vertically integrated dynamical system, (19) to (21), the appearance of the depth  $h$  in the nonlinear inertial terms is a relatively unimportant dependence (at least for the case of uniform  $h$  and with  $S$  of the order unity). If these terms are omitted, we note that the only remaining explicit appearance of the basin depth is as a coefficient of the horizontal pressure-force terms. Since the (vertically-integrated) transports  $u$  and  $v$  are essentially unaltered by depth changes in the present solutions (and are quasi-steady in the important western boundary region), we may conclude that the magnitude of the free-surface slopes  $\partial\zeta/\partial\lambda$  and  $\partial\zeta/\partial\phi$  will vary inversely with changes of the (uniform) depth  $h$ . This is confirmed by the comparative solutions for  $\zeta$  also shown in Fig. 9 (lower), where contours differing by a factor of three nearly coincide in the 400 m and 1200 m cases, while the zero contour remains in approximately the same position. We may further note that the water elevation along the boundary is also reduced by an approximate factor of three. In an ocean 4 km deep we might therefore expect a water elevation of about 10 cm across the main western boundary currents with the present wind-stress pattern.

## VI. STATISTICAL PROPERTIES OF THE SOLUTIONS

### MEAN AND VARIABILITY FIELDS

While the present integrations have been compared on a synoptic basis only at selected times, the comparisons are generally representative after an initial spin-up period of about 25 days.<sup>a</sup> Since in most cases the integrations have been carried out to 60 days, the transport and elevation solutions have been averaged over the period 30 to 60 days, and the corresponding rms (root-mean-square) variabilities determined. In general these fields portray the differences among the solutions' structure and intensity as revealed by the synoptic comparisons discussed above, and need not be presented in detail. It is of interest, however, to show these statistics for at least a reference (spherical) case.

For the case  $A = 10^8 \text{ cm}^2 \text{ sec}^{-1}$ ,  $S = 4/3$  and  $h = 400 \text{ m}$ , the distributions of the 30- to 60-day average transport and water elevation and the associated rms variabilities are shown in Fig. 10, determined from the solutions every 12 hours during this period. Here the wind stress is given by (26), and the  $60^\circ$ -longitude basin extends from  $18^\circ \text{ N}$  to  $66^\circ \text{ N}$  with a  $2^\circ$  ( $= \Delta\phi = \Delta\lambda$ ) separation between adjacent transport (or elevation) grid points. The general similarity between the average fields and the instantaneous solutions for this case shown previously in Figs. 3, 4, 7, and 8 is testimony to the near-steadiness of the major features of the solutions (and to the stability of the calculations). Seaward from the western boundary zone the average transports are the result of the passage of the successive transient Rossby waves which dominate the solutions, and in general are in an approximate geostrophic balance with the average surface elevation.

The maximum rms transport (and elevation) variability in the southwestern portion of the basin is believed to be caused by the reflection

---

<sup>a</sup>This spin-up is defined as the time required for the basin's total kinetic energy to first decrease after the major western boundary currents have reached maximum strength from an initial state of rest (see Fig. 11).



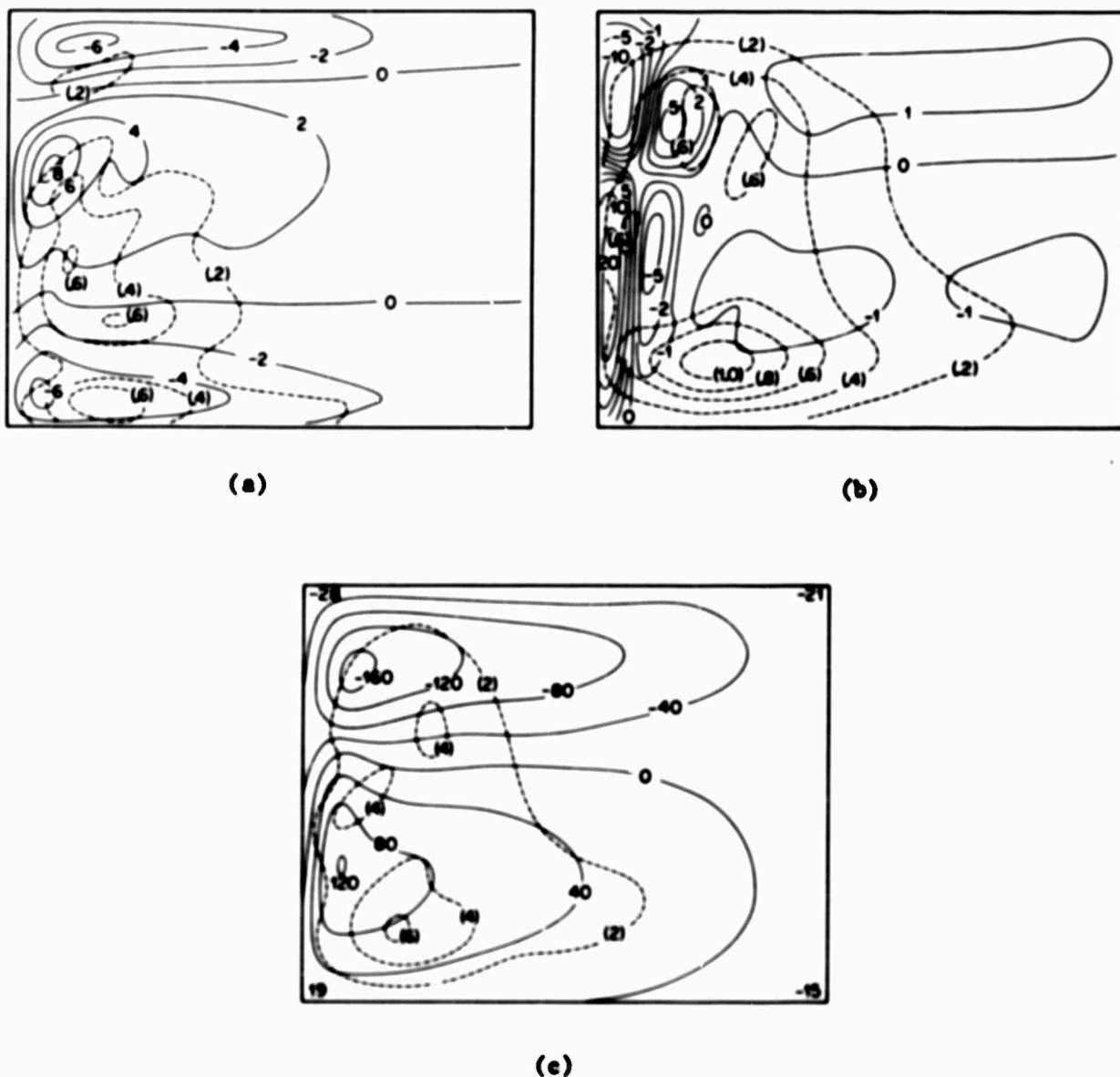


Fig. 10. The distributions of average zonal transport in  $\text{Sv} (100 \text{ km})^{-1}$  (a), meridional transport in  $\text{Sv} (100 \text{ km})^{-1}$  (b), and surface elevation in  $\text{cm}$  (c) for the period 30 to 60 days, shown by the solid isolines for a reference (spherical) case. The 30-day average currents in  $\text{cm sec}^{-1}$  are given by multiplying the transport isolines by the factor  $5/2$ . The corresponding rms (root-mean-square) variabilities during the period 30 to 60 days are shown by the dashed lines in the same units. Here  $A = 10^8 \text{ cm}^2 \text{ sec}^{-1}$ ,  $S = 4/3$ , and  $h = 400 \text{ m}$ .

from the western (and southern) shore of the transient wave energy of the major mid-latitude gyre. The role of the orientation of the western shore in such a reflection process has recently been examined by Gates (1969), who shows that the transient variability may be localized in different regions of the (western) basin by an oblique western boundary. In general the rms variability of the meridional flow is approximately twice that of the zonal motion, and is comparable with the average meridional motion itself over much of the basin outside the western countercurrents. The rms variability of the surface elevation given in Fig. 10 is compatible with the variability of the (geostrophic) meridional transport and the characteristic (reflected) transient wavelength of about 1600 km noted earlier for this case.

In the discussion of frictional effects (see Fig. 7), it was noted that the addition of bottom friction to the lateral viscous model significantly damped the amplitude of the transient Rossby waves, and reduced the magnitude of the western boundary transports. The rms variabilities in this case are some 10 to 20 percent of the values shown in Fig. 10. In the comparative  $\beta$ -plane integrations (Figs. 3 and 4) the rms variabilities are systematically larger than those shown here in the northern part of the basin, an effect caused by the  $\beta$ -plane geometry. The variabilities in the remaining comparative integrations discussed earlier (for the same basin dimensions) are all comparable to those shown for the reference case in Fig. 10.

#### ENERGY PARTITIONING

The total kinetic energy of the horizontal flow is a useful measure of the behavior of a wind-driven ocean, particularly to depict the approach of the dominant boundary currents toward a steady state (see, for example, Bryan (1963), or Veronis (1966b, 1966c). In Fig. 11 the total kinetic and potential energies are shown as a function of time for the reference (spherical) case; they were computed from the expressions

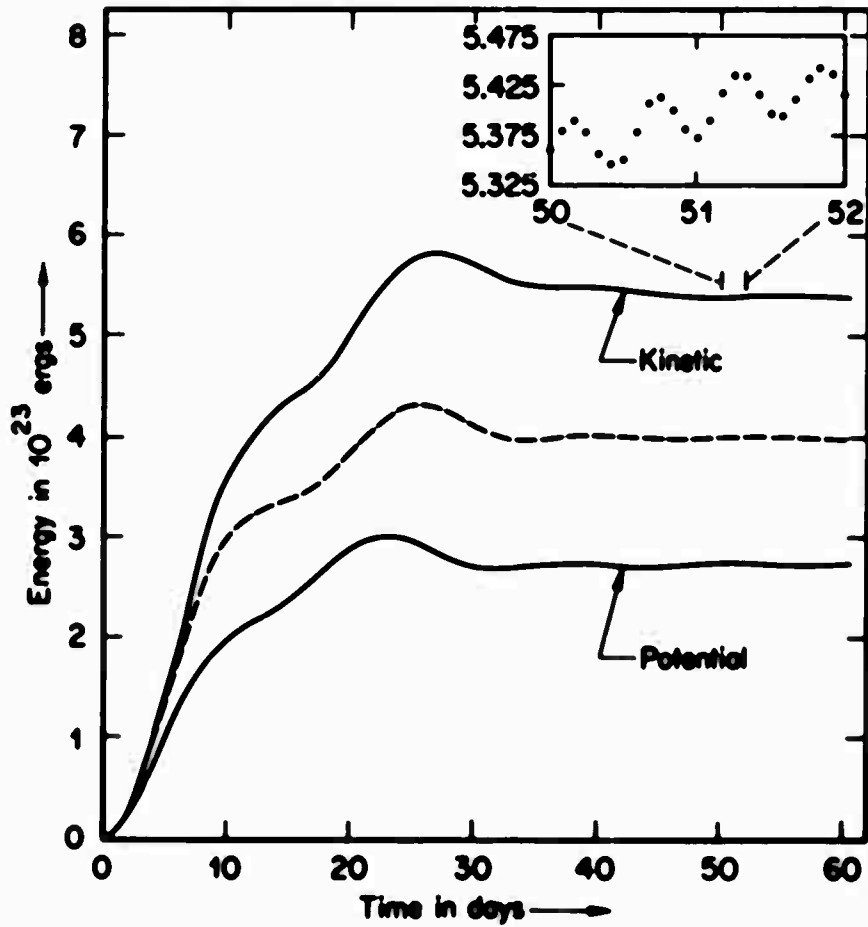


Fig. 11. The variation of the total kinetic and potential energy for the reference case of  $A = 10^8 \text{ cm}^2 \text{ sec}^{-1}$ ,  $S = 4/3$ ,  $h = 400 \text{ m}$ , and  $\Delta\lambda = \Delta\phi = 2^\circ$ . The inset shows the typical fine-scale behavior in which the kinetic energy is plotted every 2 hr. The dashed curve is the kinetic energy for the case of  $A = 2 \times 10^8 \text{ cm}^2 \text{ sec}^{-1}$ .

$$\text{total kinetic energy} = \frac{a^2 \rho_o \Delta \lambda}{4h} \sum_{ij} (\sin \phi_{j+1} - \sin \phi_{j-1}) (u_{ij}^2 + v_{ij}^2) \quad (32)$$

$$\text{total potential energy} = \frac{a^2 g \rho_o \Delta \lambda}{4} \sum_{ij} (\sin \phi_{j+1} - \sin \phi_{j-1}) \xi_{ij}^2 \quad (33)$$

where the summations extend over all transport (u,v) and elevation ( $\xi$ ) points respectively. Here a spin-up or initial energy growth period of some 24 to 26 days occurs, after which the energy shows damped oscillations with free period of the basin (approximately 13 days). Both the kinetic and potential energy characteristically fail to achieve their maximum until the second (free) period. This behavior is in contrast to that of the  $\beta$ -plane solutions, which typically reach maximum energy during the first period (see, for example, Gates [1968]). This deferred spin-up also occurs in the case of increased lateral viscosity. Superposed on these curves is a fine-scale oscillation illustrated by the inset in Fig. 11, where a period of approximately 13 hr may be identified with the passage of (long) surface gravity waves across the basin. The rms currents associated with these waves are evidently of the order of  $0.02 \text{ cm sec}^{-1}$ , and are much less than the typical currents of about  $1 \text{ cm sec}^{-1}$  associated with the transient Rossby waves.

We may also note that the potential energy is here approximately half the kinetic energy, by virtue of the relatively shallow basin depth selected. Recalling that the transports  $u$  and  $v$  are nearly independent of variations of the basin's (uniform) depth while the surface elevation varies inversely with  $h$  (see Fig. 9), the total kinetic energy (32) will vary as  $h^{-1}$  and the total potential energy (33) will vary as  $h^{-2}$ , other factors being the same. For a basin of depth  $h = 4 \text{ km}$  we could therefore expect the potential and kinetic energies to be in the ratio of about 1/20, rather than the ratio of 1/2 in the present model.

Although the bulk of the kinetic energy is evidently associated with the western boundary currents, it is of interest to make a more quantitative assessment and to examine the energy of the transient

waves in particular. In Table 4 the partitioning of the kinetic energy of both zonal and meridional motions among a zonal mean, standing zonal eddies, and transient zonal eddies is shown for the reference solution (see Figs. 10 and 11). Here the zonal average is denoted by the operator  $[( )]$ , the departure from the zonal average by  $( )^*$ , the time average (determined from the solutions every 12 hr during the period 30 to 60 days) by  $(\overline{ })$ , and the departure from the time average by  $( )'$ . In the basin as a whole approximately 71 percent of the total kinetic energy is seen to reside in the meridional motion of the standing waves, principally the western boundary current. The mean zonal motion and the zonal motion of the standing waves (which complete the major gyral circulation of the basin) account for about 28 percent of the total kinetic energy. The transient waves (here the zonally moving Rossby waves) represent only about 1 percent of the total kinetic energy, which is itself apportioned between meridional and zonal motion in approximately the ratio 3:1. In spite of this dominance of the total energy by the steady modes (the potential energy is similarly apportioned), the relatively weak transients nevertheless control the meridional transport over most of the area of the basin, as seen, for example, in Fig. 3. The data of Table 4 also show that the transient waves' contribution to the kinetic energy is greatest in the southern portion of the basin, a feature which was also noted previously.

#### ANGULAR MOMENTUM FLUX

Further insight into the role of transient planetary waves in a wind-driven circulation is afforded by the processes which are responsible for the flux of angular momentum in the basin. Table 5 shows the poleward flux of zonal angular momentum during the period 30 to 60 days for the reference case of Figs. 10 and 11 and Table 4, partitioned among the fluxes due to the zonal mean motions, the standing zonal waves, and the transient zonal waves. The standing eddies are seen to account for about 95 percent of the total momentum transport, and have a maximum flux convergence near the latitudes of the maxima of the western boundary currents (see Fig. 10); the bulk of this stationary-eddy flux convergence may therefore be associated with the western boundary current

Table 4  
KINETIC ENERGY PARTITIONING DURING THE PERIOD 30 TO 60 DAYS<sup>a</sup>

Basin Latitude (deg N)	Mode and Component Partitioning						Mode Totals				Component Totals		Total Kinetic Energy $\Sigma(1)+\dots+(6)$	
	(1)	(2)	(3)	(4)	(5)	(6)	(1)+(4)		(2)+(5)		(3)+(6)			
	Mean	Standing Waves	Transient Waves	Mean	Standing Waves	Transient Waves	Mean		Standing Waves		Transient Waves			
	$B(\bar{u})^2$	$B(\bar{u}')^2$	$B(\bar{u}'')^2$	$B(\bar{v})^2$	$B(\bar{v}')^2$	$B(\bar{v}'')^2$								
64	46.3	11.9	0.03	0	3.0	0.01	46.3	15.	15.	0.04	0.04	38.2	3.	61.
60	13.6	7.8	0.03	0	55.3	0.14	13.6	63.	63.	0.17	0.17	21.4	55.	76.
56	5.1	3.2	0.03	0	103.0	0.45	5.1	106.	106.	0.48	0.48	8.3	103.	111.
52	23.4	10.9	0.04	0	63.5	0.60	23.4	74.	74.	0.64	0.64	34.3	64.	98.
48	28.7	18.6	0.12	0	1.0	0.59	28.7	20.	20.	0.71	0.71	47.4	2.	49.
44	19.5	9.1	0.28	0	55.4	0.54	19.5	64.	64.	0.82	0.82	28.9	56.	85.
40	9.1	3.3	0.33	0	148.0	0.70	9.1	131.	131.	1.03	1.03	12.7	149.	162.
36	1.9	0.8	0.34	0	211.0	0.78	1.9	212.	212.	1.12	1.12	3.0	212.	215.
32	0.3	0.4	0.48	0	231.0	1.02	0.3	<u>231.</u>	231.	1.50	1.50	1.2	232.	233.
28	5.9	3.3	0.42	0	186.0	2.30	5.9	189.	189.	2.72	2.72	9.6	188.	198.
24	23.5	11.0	0.24	0	82.9	<u>2.80</u>	23.5	94.	94.	<u>3.04</u>	3.04	34.7	86.	121.
20	29.3	9.8	<u>1.62</u>	0	5.5	0.33	29.3	15.	15.	1.95	1.95	40.7	6.	47.
Basin Totals <sup>b</sup>	1100.	445.	13.6	0	3460.	40.6	1100.	4305.	4305.	54.2	54.2	1558.	3901.	5459.

<sup>a</sup>All energies are the totals (in  $10^{20}$  ergs) in a 1-deg latitude zonal strip extending across the basin centered at the indicated latitude, with the factor  $\delta = a^2 \sin^2 \Lambda(4\delta)^{-1} (\sin \varphi_{j+1} - \sin \varphi_{j-1})$  as in Eq. (32), where  $\Lambda = \pi/3$  is the basin's angular width and unit  $j$  corresponds to 1-deg latitude. See text for definition of transport operators.

<sup>b</sup>Based upon summation over latitude for the 16N to 16S basin, using additional data (not shown) at each 1-deg latitude.

Table 5

ANGULAR MOMENTUM FLUX DURING THE PERIOD 30 TO 60 DAYS

Basin Latitude $\varphi$ (deg N)	Momentum Flux <sup>a</sup>		Momentum Flux Convergence <sup>b</sup>		Mean Zonal Transport $[\bar{u}]$ ( $10^5 \text{ cm}^2 \text{ sec}^{-1}$ )	Mean Zonal Stress $\rho_0^{-1}[\bar{\tau}_\lambda]$ ( $\text{cm}^2 \text{ sec}^{-2}$ )	Boundary <sup>c</sup> Pressure Torque ( $\text{cm}^2 \text{ sec}^{-2}$ )
	Mean $c(\bar{u})/\bar{v}$	Standing Waves $c(\bar{u}^2/\bar{v})$	Transient Waves $c(\bar{u}^2/\bar{v})$	Mean ( $10^{-4} \text{ cm}^2 \text{ sec}^{-2}$ )	Standing Waves ( $10^{-4} \text{ cm}^2 \text{ sec}^{-2}$ )	Transient Waves ( $10^{-4} \text{ cm}^2 \text{ sec}^{-2}$ )	
64	0.19	-17.	-0.0	0.130	42.1	-0.15	-0.85
60	0.26	164.	-1.3	-0.082	201.0	-0.85	-1.15
56	-0.20	592.	-2.4	-0.047	19.7	0.32	-1.76
52	-0.32	429.	8.4	0.022	46.3	<u>1.27</u>	-2.20
48	-0.15	146.	18.4	0.036	22.8	1.41	-2.27
44	0.00	5.	26.6	0.007	5.9	0.85	-1.98
40	-0.04	-169.	<u>20.6</u>	-0.010	-2.4	0.16	-1.36
36	-0.16	-247.	27.2	0.009	24.6	-0.79	-0.53
32	0.16	27.	16.3	0.067	31.2	-0.12	0.39
28	1.25	458.	19.2	0.101	20.2	0.65	1.29
24	2.52	739	22.7	-0.005	-23.7	-0.74	1.99
20	1.23	209.	7.5	-0.142	-24.9	-0.89	2.29

<sup>a</sup>Total momentum flux across latitude  $\varphi$  in  $10^{20} \text{ gm}^2 \text{ sec}^{-2}$ , with the factor  $C = C(\varphi) = a^2 \rho \Lambda h^{-1} \cos^2 \varphi$ , where  $\Lambda = \pi/3$  is the basin's angular semi width, and  $u$  and  $v$  are the vertically integrated transports. See text for definition of transport operators.

<sup>b</sup>Found from  $(a^2 \rho \Lambda h \cos^2 \varphi)^{-1} (\bar{v}_{j+2} - \bar{v}_j)$ , where  $\bar{v}_j$  denotes the flux as in the first three columns. The convergence was calculated using flux data every 2 deg ( $\sim \Delta \varphi$ ), and thus applied 1 deg south of the indicated basin latitude.

<sup>c</sup>Found from  $-\phi(a \Lambda \cos \varphi)^{-1} (\bar{v}_E - \bar{v}_W)$ , where  $\bar{v}_E$  and  $\bar{v}_W$  are the time-averaged water elevations at the eastern and western boundaries, respectively (at the latitude  $\varphi$ ).

system. The flux of the mean zonally averaged motions  $[\bar{u}][\bar{v}]$  is relatively small because of the smallness of  $[\bar{v}]$ , which is in turn a reflection of the near steadiness of the 30- to 60-day mean flow. The transient (Rossby) waves produce a northward (positive) momentum flux over the latitudes occupied by the southern or principal gyre, with a negative flux in the northern gyre. This flux distribution is a reflection of the systematic meridional tilt of the transient waves during this period, which is characteristic of all the present solutions for basins with a meridional western boundary (see, for example, Fig. 3). The convergence of this transient-eddy flux is a maximum near the gyral boundary, where the mean zonal stress  $[\bar{\tau}_\lambda]$  is a maximum and where the mean zonal transport  $[\bar{u}]$  is strongest.

On the basis of these (and similar) calculations, the transient waves may be said to contribute in a small but systematic way to the maintenance of the mean zonal circulation in the basin, in the same sense that the atmospheric Rossby waves contribute to the maintenance of the mean zonal winds. In the atmospheric case, however, the transient eddy flux is somewhat larger than the flux of the zonal mean and standing eddies, and the flux divergence is a good measure of the mean zonal stress of the atmosphere on the earth (see, for example, Starr [1968] or Holopainen [1967]). In the ocean (or more precisely, in the present ocean model), on the other hand, the standing eddy flux is much larger than the flux of the other modes. The present oceanic case is further distinguished from the atmospheric regime by the fact that the total oceanic flux convergence by all modes (see Table 5) is apparently not an important process in the maintenance of the zonal momentum balance. Here the applied zonal wind stress  $\tau_\lambda^W$  (or  $[\bar{\tau}_\lambda^W]$ ) is approximately balanced by a net pressure torque exerted against the eastern and western walls of the basin by the wind-raised water, with the effects of lateral friction, mean meridional motion, and meridional flux convergence all smaller by several orders of magnitude.

Although a complete study of the kinetic-energy balance has not been made, the eddy momentum flux discussed above is associated with the transformation between the kinetic energy of the transient eddies



and that of the mean zonal motion. If we assume that this energy transformation is proportional to  $[\overline{u'v'}] \partial[\overline{u}]/\partial y$ , by applying the analysis of Webster (1961), for example, to the present vertically integrated model, we note from the data of Table 5 that this product is positive across virtually the entire latitudinal width of the basin. At least on the zonal average, therefore, the transient Rossby waves may be regarded as systematically supplying energy to the mean zonal motion. As was the case in the momentum balance, however, this eddy contribution is only a small part of the kinetic energy budget of the mean flow; here the dominant effects are the direct generation of the kinetic energy of the mean (zonal) motion by the zonal wind stress and its dissipation by the lateral viscosity, which occurs principally in the standing eddy which is the western boundary current itself. The presence of meridional boundaries thus makes the character of the wind-driven oceanic circulation quite different from the corresponding circulation in a laterally unbounded (global) ocean, or from the analogous barotropic atmospheric circulation regime. The large zonal boundary torque and the prominent standing (western) boundary currents, with their dominance of both the kinetic energy and momentum budgets, would presumably be absent in a zonal (circumpolar) ocean channel. The role of the transient planetary waves in the maintenance of the Antarctic circumpolar circulation, for example, might therefore be expected to be more prominent than it is in the zonally bounded major ocean basins.

## VII. CONCLUSIONS

The comparative numerical integrations presented here serve as a preliminary documentation of the behavior of a wind-driven homogeneous ocean in a basin of uniform depth on the sphere. The examination of the model's sensitivity to changes of the finite-difference grid resolution, to the use of 8-plane geometry, and to the basin size serve to illustrate the character of the purely numerical or geometrical effects inherent in such a model. From these tests we may conclude that at least a 2-deg-latitude grid-mesh resolution is required to portray satisfactorily the major current features; that the 8-plane approximation is adequate for the middle and lower latitudes; and that the western boundary current transport is approximately proportional to the zonal width of the basin. The model's response to changes of its physical parameters representing the effects of friction, nonlinearity, and water depth has also been examined. From these tests we may conclude that an increase in the magnitude of the lateral eddy viscosity generally reduces the strength of the western boundary currents; that the introduction of bottom friction reduces the intensity of both the western boundary currents and the transients; that the vertically integrated transport is only slightly affected by the inertial nonlinearity represented by simple assumed current profiles; and that an increase in the basin's (uniform) depth has little effect upon the total transport, but produces an approximately proportional decrease of the free surface water elevation and slope.

These conclusions apply to the quasi-steady circulation produced by a large-scale zonal wind stress in a basin with purely meridional and zonal boundaries. The transient planetary circulations excited by this stress are the low-order Rossby wave modes and the transients prominent in the west-central basin after about 20 days may be identified as the reflections of these waves from the western shore (Gates, 1968). These waves are responsible for a transport variation in which the rms variability of the meridional current is systematically larger than the mean meridional flow over a considerable portion of the western basin, and is usually larger than the rms variability of the zonal

current as well. Changes of the basin size or depth, or modest increases in the amount of lateral friction or inertial nonlinearity, have relatively little effect upon the transient waves in the central basin. This is in accordance with the identification of these motions with free Rossby waves, whose structure and behavior are described with good approximation by the linear inviscid equations. The amplitude of the transients, however, is markedly reduced by the introduction of bottom (Ekman) friction.

In all of the present integrations the basin has been assumed to be of uniform depth, and the wind stress has been assumed steady (as well as zonal). The introduction of time-dependent stress may be expected to enhance the role of the transient waves in the maintenance of the mean circulation through resonance and nonlinear effects (Pedlosky, 1965, 1967; Veronis, 1966a), and the presence of bottom topography may likewise exert an important influence on both the mean and transient motion in a homogeneous ocean (Holland, 1967). The results of numerical investigations of these effects will be reported separately.

REFERENCES

- Arakawa, A., 1966. Computational design for long-term numerical integration of the equations of fluid motion: two-dimensional incompressible flow, Part I. J. Comput. Phys., 1, 119-143.
- Bryan, K., 1963. A numerical investigation of a nonlinear model of a wind-driven ocean. J. Atmos. Sci., 20, 594-606.
- , and M. D. Cox, 1967. A numerical investigation of the oceanic general circulation. Tellus, 19, 54-80.
- , 1968. A nonlinear solution of an ocean driven by wind and differential heating: Parts I and II. J. Atmos. Sci., 25, 945-967, 968-978.
- Gates, W. L., 1968. A numerical study of transient Rossby waves in a wind-driven homogeneous ocean. J. Atmos. Sci., 25, 3-22.
- , 1969. The effects of western coastal orientation on Rossby wave reflection and the resulting large-scale oceanic circulation. RM-6110-RC, The Rand Corporation, Santa Monica, California, 45pp.
- Holland, W. R., 1967. On the wind-driven circulation in an ocean with bottom topography. Tellus, 19, 582-600.
- Holopainen, E. O., 1967. On the mean meridional circulation and the flux of angular momentum over the northern hemisphere. Tellus, 19, 1-13.
- Longuet-Higgins, M. S., 1964. Planetary waves on a rotating sphere. Proc. Roy. Soc., (A) 279, 446-473.
- , 1965. Planetary waves on a rotating sphere, Part II. Proc. Roy. Soc., (A) 284, 40-68.
- Munk, W. H., 1950. On the wind-driven ocean circulation. J. Meteor., 7, 79-93.
- Pedlosky, S., 1965. A study of the time dependent ocean circulation. J. Atmos. Sci., 22, 267-272.
- , 1967. Fluctuating winds and the ocean circulation. Tellus, 19, 250-267.
- Phillips, N. A., 1966a. Large-scale eddy motion in the western Atlantic. J. Geophys. Res., 71, 3883-3891.
- , 1966b. The equations of motion for a shallow rotating atmosphere and the 'traditional approximation.' J. Atmos. Sci., 23, 626-628.

Starr, V. P., 1968. Physics of Negative Viscosity Phenomena, McGraw-Hill, New York, 256 pp.

Stommel, H., 1948. The westward intensification of ocean currents. Trans. Amer. Geophys. Un., 29, 202-206.

Sverdrup, H. U., 1947. Wind-driven currents in a baroclinic ocean; with application to the equatorial currents of the eastern Pacific. Proc. Nat. Acad. Sci., 33, 318-326.

Takano, K., 1966. Effet de la sphéricité de la terre sur la circulation générale dans un océan. J. Oceanogr. Soc. Japan, 22, 255-263.

Veronis, G., 1963. On the approximations involved in transforming the equations of motion from a spherical surface to the  $\beta$ -plane, I. Barotropic systems. J. Mar. Res., 21, 110-124.

-----, 1966a. Generation of mean ocean circulation by fluctuating winds. Tellus, 18, 67-76.

-----, 1966b. Wind-driven ocean circulation - Part I. Linear Theory and perturbation analysis. Deep-Sea Res., 13, 17-29.

-----, 1966c. Wind-driven ocean circulation - Part 2. Numerical solutions of the nonlinear problem Deep-Sea Res., 13, 31-55.

Webster, F., 1961. The effect of meanders on the kinetic energy balance of the Gulf Stream. Tellus, 13, 392-401.

## DOCUMENT CONTROL DATA

1. ORIGINATING ACTIVITY  The Rand Corporation		2a. REPORT SECURITY CLASSIFICATION UNCLASSIFIED	
		2b. GROUP	
3. REPORT TITLE STUDIES IN CLIMATE DYNAMICS FOR ENVIRONMENTAL SECURITY: NUMERICAL STUDIES OF TRANSIENT PLANETARY CIRCULATIONS IN A WIND-DRIVEN OCEAN ON THE SPHERE			
4. AUTHOR(S) (last name, first name, initial) Gates, W. Lawrence			
5. REPORT DATE April 1970	6a. TOTAL NO. OF PAGES 62	4b. NO. OF REFS. 24	
7. CONTRACT OR GRANT NO. DAHC15 67 C 0141	8. ORIGINATOR'S REPORT NO. RM-6211-ARPA		
9a. AVAILABILITY/LIMITATION NOTICES DDC-1		9b. SPONSORING AGENCY Advanced Research Projects Agency	
10. ABSTRACT A numerical investigation of a bounded ocean basin on the spherical earth, with particular attention directed to the role of planetary circulations. The time-dependent primitive equations are solved for a shallow, wind-driven, homogeneous ocean in a basin of uniform depth on the sphere. In a series of comparative numerical solutions, it is shown that at least a 2-deg resolution is needed to resolve the western boundary currents adequately and to avoid undue distortion of the transient Rossby waves. Although the transient Rossby waves systematically produce a momentum flux convergence at the latitude of the maximum eastward current, this is only a relatively small contribution to the zonal oceanic momentum balance; the bulk of the mean zonal stress is balanced by a nearly stationary net pressure torque exerted against the meridional boundaries by the wind-raised water.		11. KEY WORDS  Atmosphere Meteorology Climate Oceanography	